Journal of Volcanology and Geothermal Research 415 (2021) 107249

Contents lists available at ScienceDirect

Journal of Volcanology and Geothermal Research

journal homepage: www.elsevier.com/locate/jvolgeores

Formation of Stanley Patch volcanic cone: New insights into the evolution of Deception Island caldera (Antarctica)

J. Hopfenblatt [a,b], A. Geyer [a,*], M. Aulinas [b], A.M. Álvarez-Valero [c], G. Gisbert [d], G. Kereszturi [e], G. Ercilla [f], M. Gómez-Ballesteros [g], A. Márquez [h], D. García-Castellanos [a], D. Pedrazzi [a], H. Sumino [i], A. Höskuldsson [j], S. Giralt [a], C. Angulo-Preckler [k,l]

[a] Geosciences Barcelona, Geo3Bcn, CSIC, Lluis Sole i Sabaris s/n, 08028 Barcelona, Spain
[b] Departament de Mineralogia, Petrologia i Geologia Aplicada, Universitat de Barcelona, Marti Franques s/n, 08028 Barcelona, Spain
[c] Departamento de Geología, Universidad de Salamanca, 37008 Salamanca, Spain
[d] Instituto de Geociencias, CSIC-UCM, Severo Ochoa 7, 28040 Madrid, Spain
[e] Volcanic Risk Solutions, School of Agriculture and Environment, Massey University, Palmerston North, New Zealand
[f] Instituto de Ciencias del Mar, ICM-CSIC, Continental Margin Group, Paseo Marítimo de la Barceloneta, 37-49, 08003 Barcelona, Spain
[g] Instituto Español de Oceanografía, C/Corazón de María 8, 28002 Madrid, Spain
[h] Área de Geología, ESCET, Universidad Rey Juan Carlos, 28933 Móstoles, Madrid, Spain
[i] Department of General Systems Studies, Graduate School of Arts and Sciences, University of Tokyo, Japan
[j] Nordic Volcanological Center, Institute of Earth Sciences, University of Iceland, Sturlugata 7, 101 Reykjavik, Iceland
[k] Norwegian College of Fishery Science, UiT The Arctic University of Norway, Tromsø, Norway
[l] IRBio (Research Institute of Biodiversity), Barcelona, Spain

ARTICLE INFO

Article history:
Received 22 December 2020
Received in revised form 19 March 2021
Accepted 12 April 2021
Available online 16 April 2021

Keywords:
Deception Island
South Shetland Islands
Antarctic volcanism
Caldera flooding
Caldera evolution
Seismic profiles

ABSTRACT

Deception Island (South Shetland Islands) is one of the most active volcanoes in Antarctica, with more than 20 explosive eruptive events registered over the past centuries. Recent eruptions (1967, 1969, and 1970) and volcanic unrest episodes (1992, 1999, and 2014–2015) demonstrate that volcanic activity is likely occurring in the future. This is of special concern for scientists, logistic personnel, and tourists, since the South Shetland Islands are an important tourist destination and host numerous year-round and seasonal scientific stations and base camps. Significant efforts have been made to understand the complex magmatic and volcanic evolution of Deception Island with special interest on its subaerial part. However, studies on submerged volcanic cones within Port Foster, the sea-flooded part of Deception Island's caldera depression, are comparatively scarce. Here, we provide a full characterization of Stanley Patch volcano, the largest of these volcanic edifices. Estimated morphometric parameters based on new multibeam bathymetric data, supported by petrographic and chemical observations from rock samples collected on the crater rim, reveal that Stanley Patch volcano grew in a subaerial environment. This result, combined with previous findings and new sedimentological evidence from our ultra-high resolution seismic profiles, allow to further detail the island's geologic evolution since the caldera collapse. We conclude that the complete flooding of Port Foster could have only occurred after the formation of Stanley Patch volcano, i.e. during the last ~2000 years, and in a time period of a few days or less.

1. Introduction

Deception Island (South Shetland Islands) is among the most active volcanoes in Antarctica with a record of more than 20 explosive eruptions in the last centuries (e.g., Orheim, 1972; Roobol, 1982; Smellie, 2002a; Geyer, 2021). It consists of a composite volcano, whose central part is occupied by a c. 8.5 × 10 km collapse caldera, elongated in NW-SE direction (Fig. 1a). The caldera-forming eruption, with 30–60 km^3 of erupted magma (dense rock equivalent), has been estimated to be comparable in size to some of the largest eruptions occurring on Earth over the past several millennia (e.g., 1883 Krakatoa eruption) (Martí et al., 2013). Port Foster, the sea-flooded part of the caldera depression, has smaller dimensions (c. 6 × 10 km) due to the numerous post-caldera eruptions occurred around the caldera wall margins (e.g., Pedrazzi et al., 2020; Smellie, 1988, 2002a; Geyer et al., 2021) (Fig. 1b). The recorded historical volcanic activity, the most recent eruptive events (1967, 1969, and 1970), and the episodes of unrest which occurred in 1992 (Ibáñez et al., 2003b), 1999 (Ibáñez et al., 2003a), and 2014–2015 (Almendros et al., 2018; Berrocoso et al., 2018), undoubtedly categorize Deception Island as a very active volcano. This leads directly to a

* Corresponding author.
E-mail address: ageyer@geo3bcn.csic.es (A. Geyer).

https://doi.org/10.1016/j.jvolgeores.2021.107249

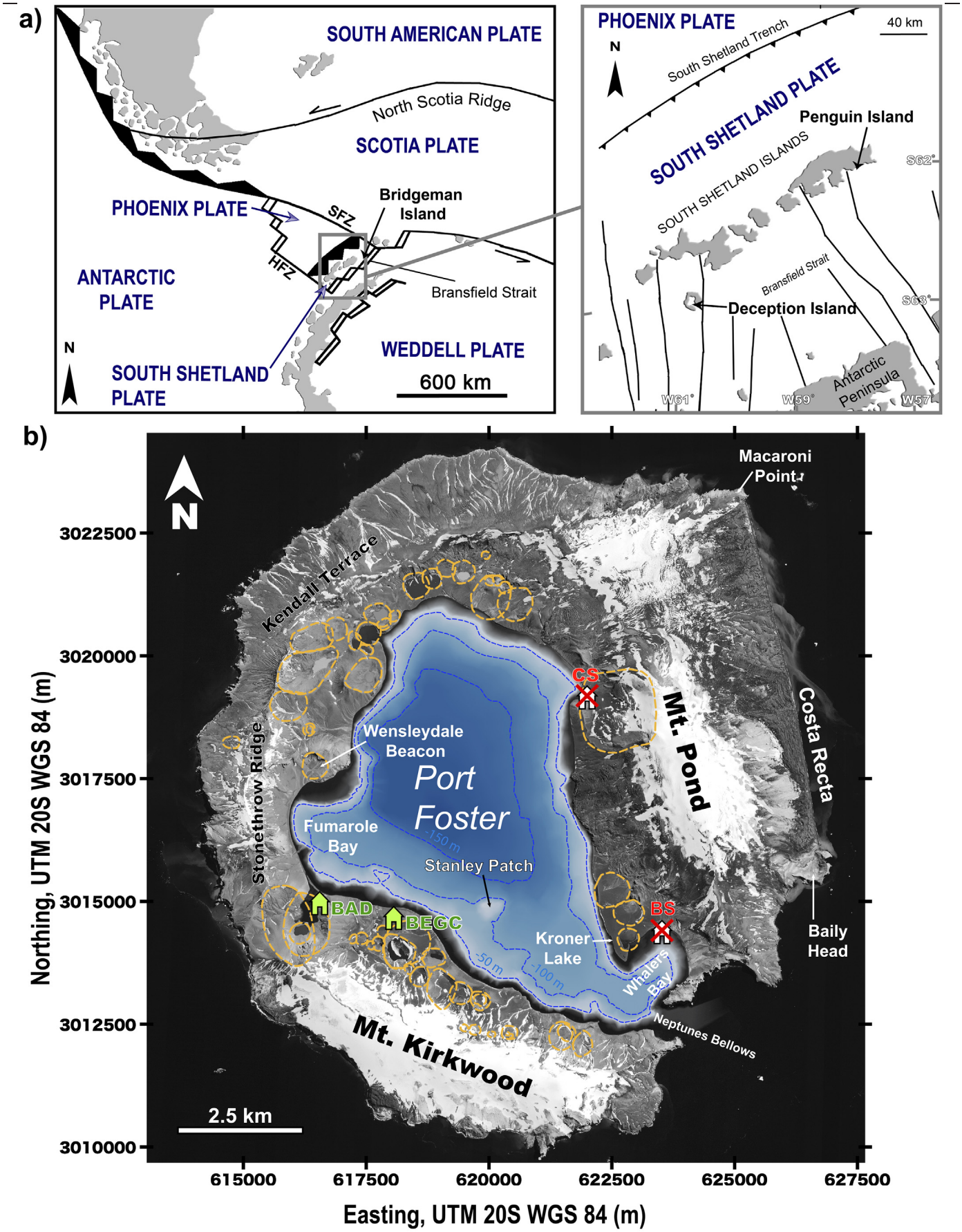
a)
SOUTH AMERICAN PLATE
North Scotia Ridge
SCOTIA PLATE
PHOENIX PLATE
SFZ
HFZ
Bridgeman Island
ANTARCTIC PLATE
Bransfield Strait
WEDDELL PLATE
SOUTH SHETLAND PLATE
600 km
N
PHOENIX PLATE
South Shetland Trench
40 km
SOUTH SHETLAND PLATE
Penguin Island
SOUTH SHETLAND ISLANDS
S62°
Bransfield Strait
Deception Island
S63°
Antarctic Peninsula
W61°
W59°
W57°
b)
Macaroni Point
Kendall Terrace
Stonethrow Ridge
Wensleydale Beacon
Port Foster
Fumarole Bay
-150 m
Stanley Patch
CS
Mt. Pond
Costa Recta
BAD
BEGC
BS
Kroner Lake
-50 m
-100 m
Whalers Bay
Neptunes Bellows
Baily Head
Mt. Kirkwood
2.5 km
3022500
3020000
3017500
3015000
3012500
3010000
615000
617500
620000
622500
625000
627500
Northing, UTM 20S WGS 84 (m)
Easting, UTM 20S WGS 84 (m)

significant socio-economic problem since the South Shetland Islands are an important tourist destination and host numerous year-round and seasonal scientific stations and base camps (e.g., Bartolini et al., 2014; Bender et al., 2016). Hence, even a moderate eruption (e.g., Volcanic Explosivity Index - VEI of 3–4) occurring in the near future on the island will pose far-reaching volcanic hazards and substantial economic losses and consequences for global aviation safety in the Southern Hemisphere (e.g., Bartolini et al., 2014; Geyer et al., 2017; Smellie, 2002c). Therefore, completing our knowledge about the island's evolution is fundamental to untangle the potential for future volcanic activity, and to significantly improve our understanding of the monitoring data recorded during a volcanic crisis in order to better forecast future unrest.

Important efforts have been made to understand the complex magmatic and volcanic evolution of Deception Island with special interest on its subaerial part (e.g., Agusto et al., 2007; Aparicio et al., 1997; Baker, 1969; Baker et al., 1969, 1975; Baker and McReath, 1971; Baraldo and Rinaldi, 2000; Birkenmajer, 1992; Galé et al., 2014; Geyer et al., 2019; González-Ferrán et al., 1971; González-Ferrán and Katsui, 1970; Hawkes, 1961; Martí et al., 1996; Roobol, 1980; Smellie, 1988, 2001, 2002b; Smellie et al., 2002). However, studies on submerged cones within the Port Foster are comparatively scarce (e.g., Barclay et al., 2009; López-Martínez et al., 2000; López-Martínez and Serrano, 2002; Rey et al., 1995, 1997; Somoza et al., 2004; Smellie, 2021).

During the 2017–2018 Spanish Antarctic Campaign, a geophysical study was carried out in Port Foster with special focus on Stanley Patch volcano, the largest volcanic cone located in the southern sector of the bay (Figs. 1b and 2a). A new multibeam swath bathymetry was obtained together with several high-resolution parametric seismic profiles of Port Foster's shallow sub-bottom structure (Gómez-Ballesteros et al., 2018). Additionally, and for the first time, juvenile rock samples were collected from Stanley Patch by SCUBA diving (Angulo-Preckler et al., 2021). In this study, we present a morphological characterization of this volcanic edifice based on these new multibeam bathymetric data. Results obtained, supported by the petrographic description and chemical analyses of the collected rock samples, allow us to shed new light on the eruptive event that lead to the formation of Stanley Patch volcano. Then, this information is combined with sedimentological evidence from our new ultra-high resolution seismic profiles and numerical flood models, to further detail the geological evolution of Deception Island since the caldera collapse.

2. Deception Island's geological overview

2.1. Geological setting, magmatic and volcanic evolution

Deception Island is located at the south-western end of the Bransfield Strait (e.g., Catalán et al., 2013, 2014; Grad et al., 1992) (Fig. 1a), a ~ 4 Ma old extensional structure interpreted to be the consequence of back-arc extension linked to subduction of the Phoenix Plate beneath the Antarctic Plate (Barker, 1982; McCarron and Larter, 1998). Quaternary magmatism, connected to rifting and back-arc basin formation, is mostly concentrated on Deception, Penguin, and Bridgeman Islands (e.g., Birkenmajer et al., 1990; Haase et al., 2012; Hole et al., 1994; Smellie, 2021). The normal magnetic polarity of all Deception Island's exposed rocks indicates that these are younger than 0.75 Ma (Valencio et al., 1979), and K—Ar data (Keller et al., 1992) point to 0.2 Ma. Paleomagnetic data suggest ages of c. 8300 years for the caldera collapse that strongly marked the island's morphology and subsequent volcanic evolution (Oliva-Urcia et al., 2015). However, more recent findings indicate that the most likely age for the caldera-forming event is 3980 ± 125 calibrated years Before Present (BP) based on tephrochronology, sedimentology studies and ^{14}C dates (Antoniades et al., 2018).

Previous to the caldera collapse, volcanic activity led to the formation of multiple shoaling seamounts and a main subaerial volcanic edifice (Smellie, 2002a) (Fig. 2b). During the caldera-forming event, a several tens of meters thick sequence of pyroclastic density current deposits, known as the Outer Coast Tuff Formation (OCTF) was emplaced (Martí et al., 2013; Smellie, 2001, 2002a) (Fig. 2a and b). Post-caldera eruptive events, predominantly located along the structural borders of the caldera and the interior of Port Foster (Fig. 1b), have mainly consisted of hydromagmatic eruptions with variable intensity and explosivity degree mostly depending on the amount and provenance of water (i.e., aquifer, sea, and/or ice/snow melting) that interacted with the rising or erupting magma (e.g., Baker et al., 1975; Pedrazzi et al., 2014, 2018, 2020; Smellie, 2002b). Historic eruptions, generally <0.1 km^3 in volume and a VEI of 2–3 (Baker et al., 1975), have been concentrated in eruptive clusters (e.g., 1818–1828, 1906–1912) with several temporally closely spaced events, separated by decades of quiescence (e.g., 1912–1967) (Orheim, 1972; Roobol, 1982; Smellie, 2002a).

2.2. Port Foster: geomorphology and internal structure

Port Foster is assumed to have formed just after the caldera-forming event by marine inundation of the collapsed depression via gaps in the caldera rim created by local sector collapse and/or volcanic events (e.g., Aparicio et al., 1997; Smellie and López-Martínez, 2002a). The bay is open to the sea by a narrow and shallow entrance (< 500 m wide and < 25 m deep) at Neptunes Bellows (Fig. 1b) and is composed of three sub-basins (Cooper et al., 1998; Paredes et al., 2006; Rey et al., 2002; Fig. 3): (i) sub-basin 1 (165 m maximum water depth) that occupies the entire northern half of the bay; (ii) sub-basin 2 (< 110 m water depth) that extends from east of Stanley Patch into Whalers Bay; and (iii) sub-basin 3 (100–120 m water depth), a smaller basin in the Fumarole Bay. Whereas the limit between the sub-basins 2 and 3 is subdued, sub-basin 1 is delimited on its south and south-western side by a striking ENE-dipping monoclinal structure related to a major NNW-SSE-trending fault (Cooper et al., 1998; López-Martínez and Serrano, 2002) (Fig. 3a–c).

Previous seismic studies within Port Foster have imaged geological structures at the topmost 300 m below the sea floor in the central part of the caldera depression (e.g., Kowalewski et al., 1990; López-Martínez and Serrano, 2002; Rey et al., 1995, 1997, 2002; Somoza et al., 2004). The basin infilling comprises three seismic units A, B, and C, from older to younger (Rey et al., 1995, 1997), separated by unconformities interpreted to be individual deformation events that disturbed the geometry of the sedimentary materials (Fig. 3d and e) (Kowalewski et al., 1990; López-Martínez and Serrano, 2002; Rey et al., 1995, 1997). Unit A is interpreted as the intra-caldera facies of the OCTF deposited during the caldera-forming eruption (e.g., Martí et al., 2013; Rey et al., 2002). It gently dips to the south-west and is overlain by two major post-caldera sedimentary units B and C, both divided into several sub-units (Fig. 3d and e). Their distribution and strata pattern suggest either that basinal subsidence occurred along the monocline at greater rates than local sedimentation, or that subsidence in the south-western part of the basin was accompanied by uplift in the north-east (Fig. 3e) (Kowalewski et al., 1990; Rey et al., 2002). Indeed, during the last decades, ground deformation monitoring (e.g., Almendros et al., 2015; Fernandez-Ros et al., 2007; Rosado et al., 2019) and the analysis of bathymetric variations (Barclay

Fig. 1. a) Simplified regional tectonic map and location of the South Shetland Islands (modified from Martí et al., 2013). HFZ (Hero Fracture Zone), SFZ (Shetland Fracture Zone). b) Deception Island orthophotomap with bathymetric data (data obtained from Spatial Data Infrastructure for Deception Island SIMAC, Torrecillas et al., 2006). BAD: Base Antártica Decepción (Argentinean scientific base); BEGC: Base Española Gabriel de Castilla (Spanish scientific base); BS: Remains of the British scientific base; and CS: Remains of the Chilean scientific base. Post-caldera volcanic craters (orange lines) are indicated based on Smellie and López-Martínez (2002b).

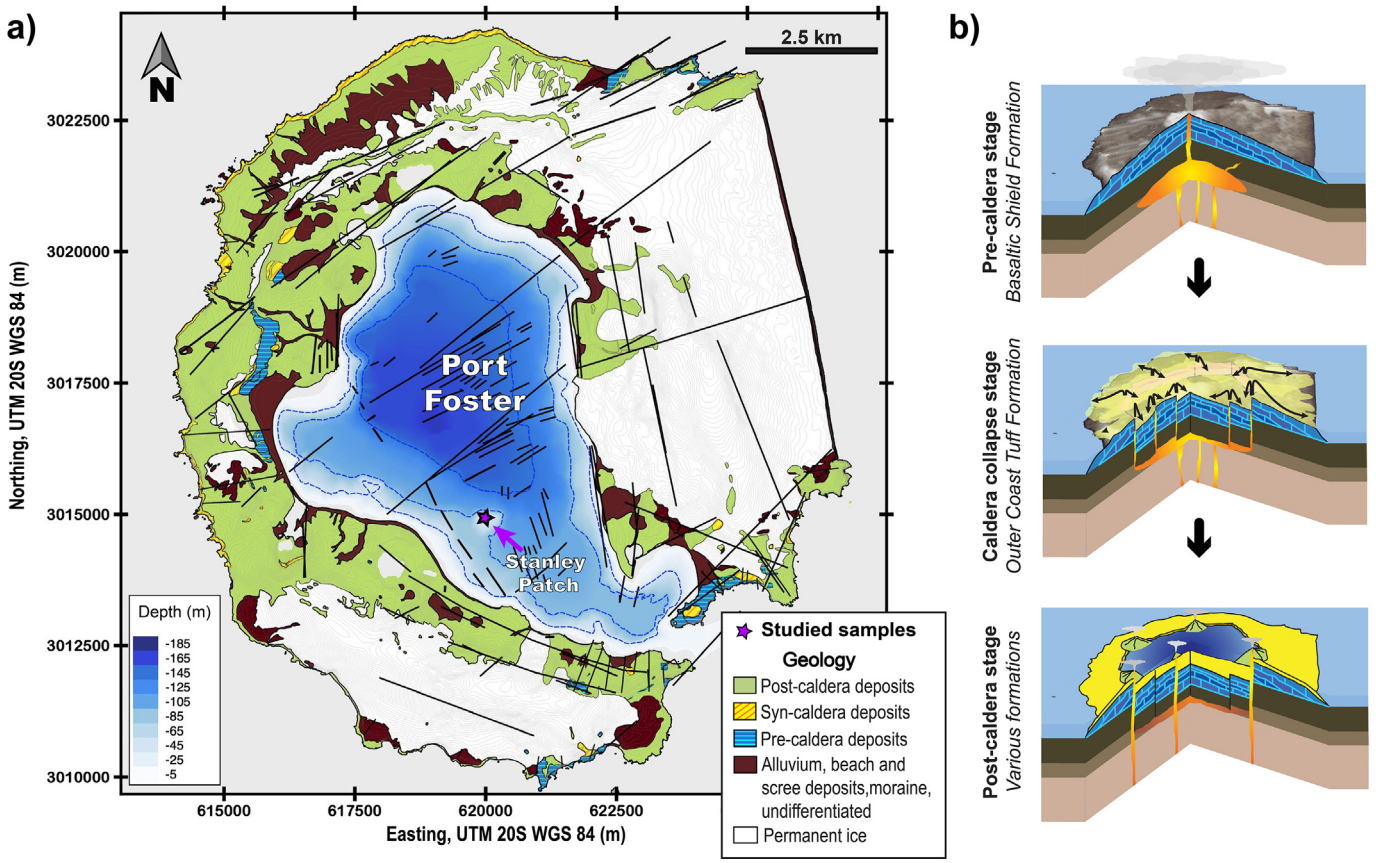
a)
N
2.5 km
Port Foster
Stanley Patch
Depth (m)
-185
-165
-145
-125
-105
-85
-65
-45
-25
-5
Studied samples
Geology
Post-caldera deposits
Syn-caldera deposits
Pre-caldera deposits
Alluvium, beach and scree deposits,moraine, undifferentiated
Permanent ice
Northing, UTM 20S WGS 84 (m)
Easting, UTM 20S WGS 84 (m)
3022500
3020000
3017500
3015000
3012500
3010000
615000
617500
620000
622500
b)
Pre-caldera stage
Basaltic Shield Formation
Caldera collapse stage
Outer Coast Tuff Formation
Post-caldera stage
Various formations

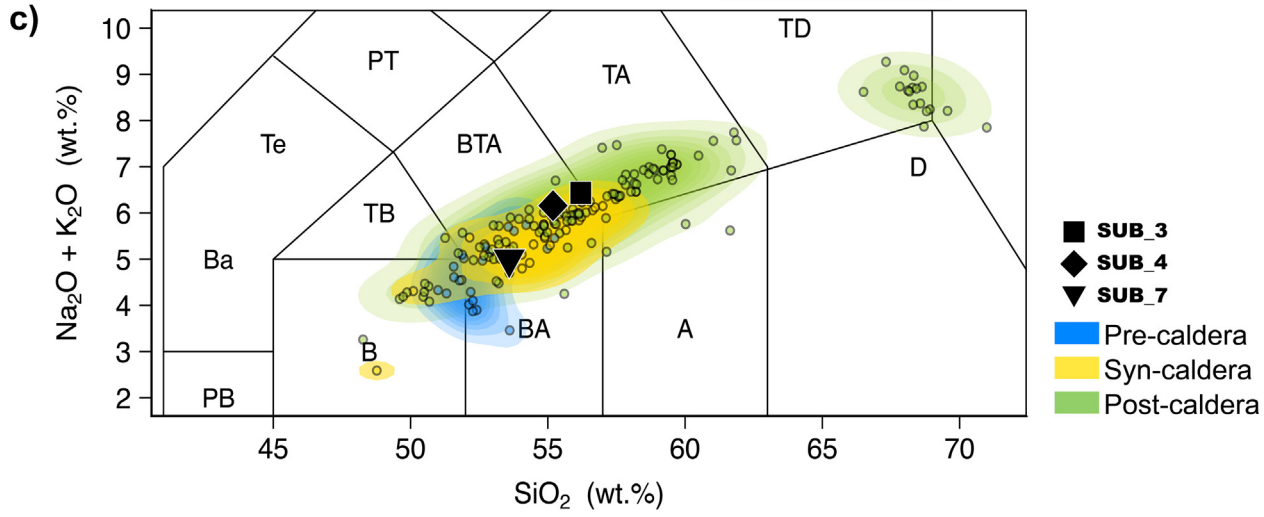
c)
PT
TA
TD
Te
BTA
D
TB
Ba
BA
A
B
PB
Na2O + K2O (wt.%)
SiO2 (wt.%)
SUB_3
SUB_4
SUB_7
Pre-caldera
Syn-caldera
Post-caldera

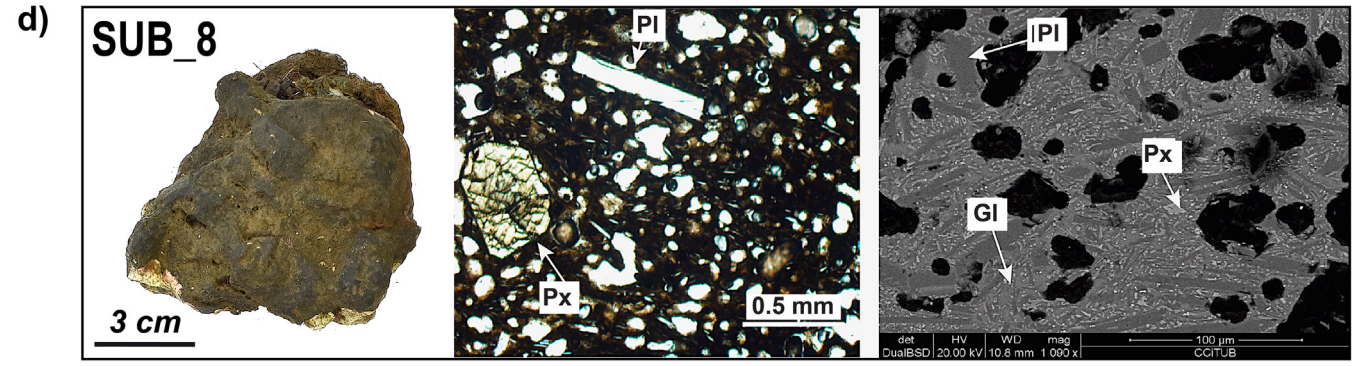
d)
SUB_8
3 cm
Pl
Px
0.5 mm
Gl

et al., 2009; Cooper et al., 1998) have shown that, in the past, the basin's floor has experienced notorious deformation episodes including uplift/subsidence stages.

Several submarine pyroclastic cones dot the Port Foster seafloor (López-Martínez and Serrano, 2002; Rey et al., 1995, 1997). These volcanic edifices show an arcuate NNW-SSE alignment and are characterized by relatively steep slopes and a dome-like or cone morphology, the largest one being Stanley Patch volcano first identified as a volcanic edifice in 1987 (Figs. 1, 3 and 4) (British Antarctic Survey, 1987; López-Martínez and Serrano, 2002).

3. Methods

3.1. Fieldwork and geophysical study

Fieldwork, including rock sample collection and the geophysical study, was carried out during the 2017–2018 Spanish Antarctic Campaign and the Antarctic GALILEO-IHM cruise aboard the R/V Hespérides (2017/2018) (Gómez-Ballesteros et al., 2018; Angulo-Preckler et al., 2021). The swath bathymetry was acquired by a multibeam echosounder system (Kongsberg EM-1002) operating 111 beams at 95 kHz frequency, with approximately 2° beam width. Surveys were carried out by the Marine Hydrographic Institute (IHM) in 2012, 2017, and 2018. Undertaken to meet International Hydrographic Organization (IHO) standards for multibeam surveying, the different surveys were positioned to insonify 100% of the seafloor with a 33% overlap between them. The resulting data set was processed using Caris Hips & Sips V.7.1 software and interpolated to an 8 × 8 m sided regular grid in Port Foster and a 4 × 4 m sided regular grid for Stanley Patch volcano, providing virtually continuous coverage of the entire survey area with high spatial resolution. Then, Digital Elevation Models (DEM) surfaces were created with QGIS software version 3.10 "A Coruña" (http://www.qgis.org/) and GRASS GIS software version 7.6 (http://grass.osgeo.org) (Figs. 3a and 4a).

Parametric seismic profiles were obtained with a hull-mounted TOPAS PS 018 high-resolution parametric sounder designed for sub-bottom profiling with very high spatial resolution in water depths from less than 20 m to full ocean depth. The +80% relative bandwidth, low frequency signal is generated in the water column by non-linear interaction between two high frequency signals (centered symmetrically around 18 kHz). The seismic profiles obtained were recorded working in high-penetration mode, by transmission of a Chirp wave (LFM), trying at all times not to interfere with the EM122 multibeam echosounder signal. Normal transmission frequencies vary from 2.0 kHz for the initial and 5 kHz for the final, with a pulse length of 10 ms, and transmitted at a 1500 ms internal mode trigger interval (Table S1). The record length was 400 ms at a sampling rate of 16.0 kHz. The deconvolution and initial 2 kHz filtering (HP filter) of the signal have always been applied in this Chirp mode. The TVG ramps normally used during the acquisition have been 0.78 d/ms between the bottom and 5.4 ms depth, 0.77 d/ms between 5.4 and 25.9 ms, and 0.14 d/ms after 35.6 ms. The seismic profiles (Figs. 5a, 6a–c and S1) are presented in two-way time and have been analyzed with the Kingdom Suite (Version 8.4) software to identify, define the top and base, and interpret sedimentary units and acoustical facies. For conversion depth in double-time depth (TWT) to depths (in distance), seismic velocities between 1600 and 1900 m/s as typical for volcanic sediments (Hamilton, 1970; Johnston et al., 2015) have been considered. For specific seismic units, the depth points (in ms) of base and top extracted from the seismic profiles are imported into GRASS GIS and interpolated to 3D surfaces with the *v.surf.bspline* function, which performs a bilinear/bicubic spline interpolation with Tykhonov regularization (e.g., Fathi and Maleki Shoja, 2018). Then, the *r.contour* function is applied to calculate the isobaths (Fig. S2). Additionally, isopach maps (in ms) of the sedimentary units can be created by difference from the generated base and top 3D surfaces (Fig. 6d).

3.2. Geomorphometrical methods

The morphological parameters of Stanley Patch volcano were obtained from the 4 × 4 m grid size DEM. Shaded relief (Fig. 4b and d) and slope angle maps (Fig. 4c) were created with QGIS from the DEM to manually delineate the cone base outline and crater rim both identified by a break-in-slope (Fig. 4a). The pre-eruptive basal surface was obtained by interpolating the elevation data points around the volcanic cone (Fig. S3) with the *v.surf.bspline* function of GRASS GIS. The average slope of the basal plane (Sb_{mean}) was obtained by applying a linear regression to the elevation points obtained along a profile aligned along the maximum dip direction of the basal surface (Fig. S3). Complementarily, a statistical analysis with the R-Studio software (https://www.rstudio.com/) (R Core Team, 2014) was carried out to obtain data of mean, median, maximum and minimum slopes, and standard deviation, for both the crater and cone flanks. The morphometric parameters estimated from the DEM are summarized in Table 1 and Figs. 4d and e.

3.3. Geochemical, petrological and stable isotopes analyses

We collected a total of 21 rock samples of 3–15 cm in diameter size at the southern side of the crater rim (Angulo-Preckler et al., 2021). From these, we have selected only those juvenile fragments of larger size (> 5 cm) and less weathered appearance (5 in total, SUB_3 to SUB_5, SUB_7, and SUB_8) for geochemical and petrographic analyses (Table S2, Fig. S4). Petrographic characteristics of all samples were determined using an optical microscope, a Zeiss Axiophot at the Universitat de Barcelona (UB). Detailed studies of microtextures were performed using a scanning electron microscope SEM Quanta 200 FEI, XTE 325/D8395 at the Scientific and Technological Centre of UB (CCiTUB) (http://www.ccit.ub.edu/EN/home.html). Whole rock major and trace element compositions were analyzed by X-Ray Fluorescence (XRF) using a ThermoARL Advant'XP+ sequential X-ray spectrometer at the GeoAnalytical Lab at Washington State University (WSU) (https://environment.wsu.edu/facilities/geoanalytical-lab/). Trace elements and Rare Earth Elements (REE) were also analyzed on the same samples by Inductively Coupled Plasma—Mass Spectrometry (ICP-MS) using an Agilent 7700 at WSU. Major element glass and mineral chemistry was also analyzed on thin sections using a JEOL JXA-8230 electron microprobe at the CCiTUB. The instrument was calibrated previous to each session using primary natural and synthetic standards from P and H developments Ltd. (https://www.pandhdevelopments.com/). Diopside or albite (Si), corundum (Al), orthoclase (K), rutile (Ti), wollastonite (Ca), periclase (Mg), albite (Na), Fe_2O_3 (Fe), rhodonite (Mn) and Cr_2O_3 (Cr), NiO (Ni) and celestine (Sr) were used as primary standards. In the case of mineral phases, detection limit of most elements at 2sigma confidence level is below 0.03 wt% with exception of Na (0.04 wt%), Cr (0.08 wt%) and Sr (0.14 wt%). Detection limits for glass are below 0.05

Fig. 2. a) Simplified geological map of Deception Island (modified from Martí et al., 2013; Smellie and López-Martínez, 2002b) showing the distribution of the two main tectonic fault sets, NW-SE and NE-SW according to De Rosa et al. (1995). Data obtained from Spatial Data Infrastructure for Deception Island SIMAC (Torrecillas et al., 2006) and López-Martínez et al. (2000). b) The three cartoons present the volcanic evolution of the island starting with the composite volcano formation, followed by the caldera collapse, and finishing with the post-caldera eruptive episodes (modified from Martí et al., 2013). c) Total Alkali vs. Silica diagram (TAS) (Le Bas et al., 1986) for Deception Island rock samples (see Geyer et al., 2019) and the rock samples of Stanley Patch volcano (See Table S3). Major elements are normalized to 100% (anhydrous) with Fe distributed between FeO and Fe_2O_3 following Middlemost (1989). d) Example of one of the rock samples collected at Stanley Patch volcano. Plane light (center) and scanning electron (right) microscope images of the samples are also included. GI: Interstitial glass; Pl: Plagioclase; Px: Pyroxene.

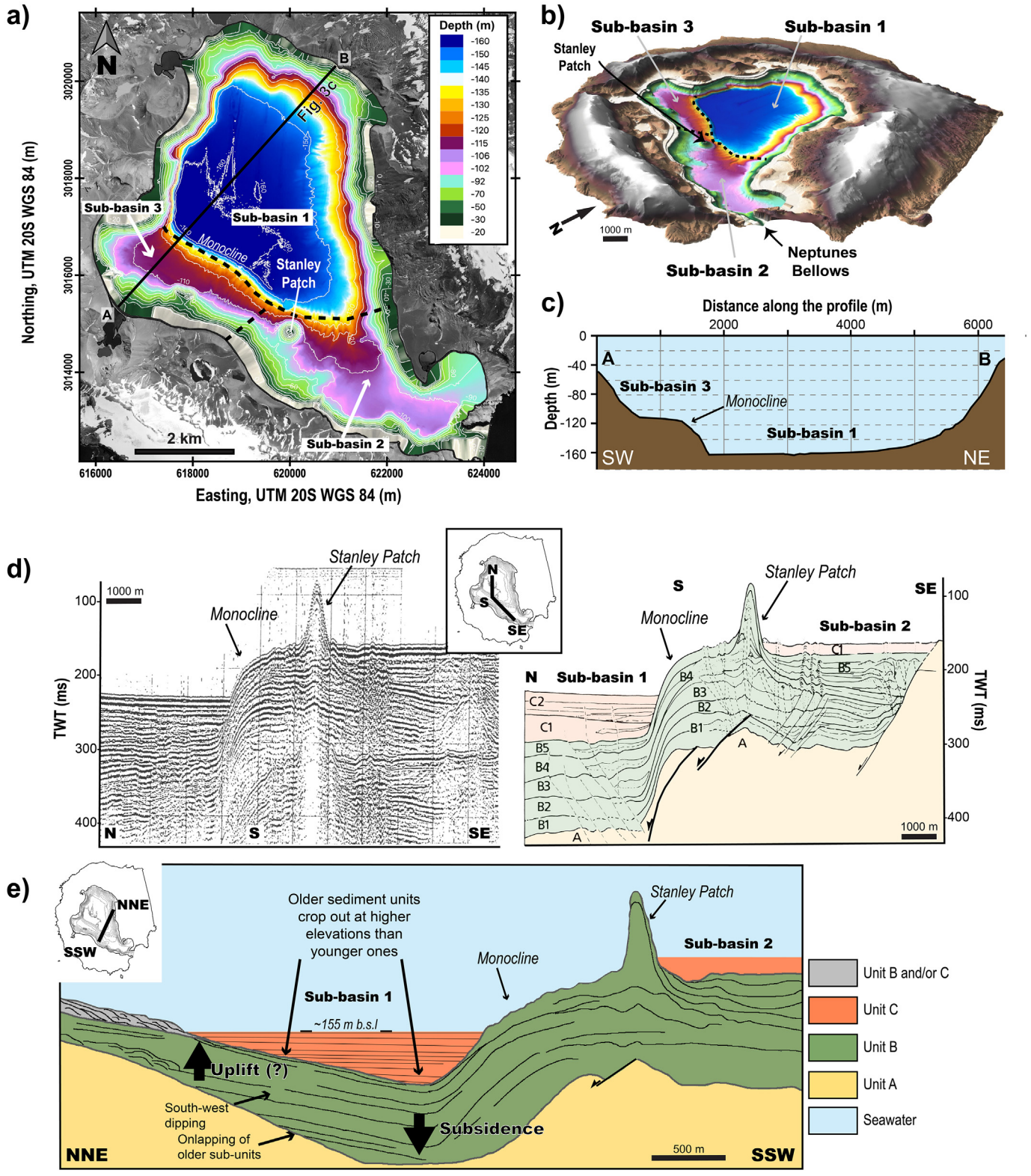

Fig. 3. a) Deception Island orthophotomap (data obtained from Spatial Data Infrastructure for Deception Island SIMAC, Torrecillas et al., 2006) and Digital Elevation Model of Port Foster obtained during the 2012 and 2017–2018 Spanish Antarctic Campaign by the Marine Hydrographic Institute. The limits of the different sub-basins are also indicated. b) 3D shaded relief map of Port Foster and Deception Island. Vertical exaggeration is ×1.5; c) bathymetric profile of Port Foster. The location is shown in a); d) composite seismic reflection profile (Sparker) (left) and its interpretation (right) obtained across Port Foster, showing the seismo-acoustic depositional units A, B and C described in the text (after Rey et al., 1995); e) simplified schematic composite section across Port Foster (modified from Kowalewski et al., 1990; Rey et al., 1995; Smellie, 2002a).

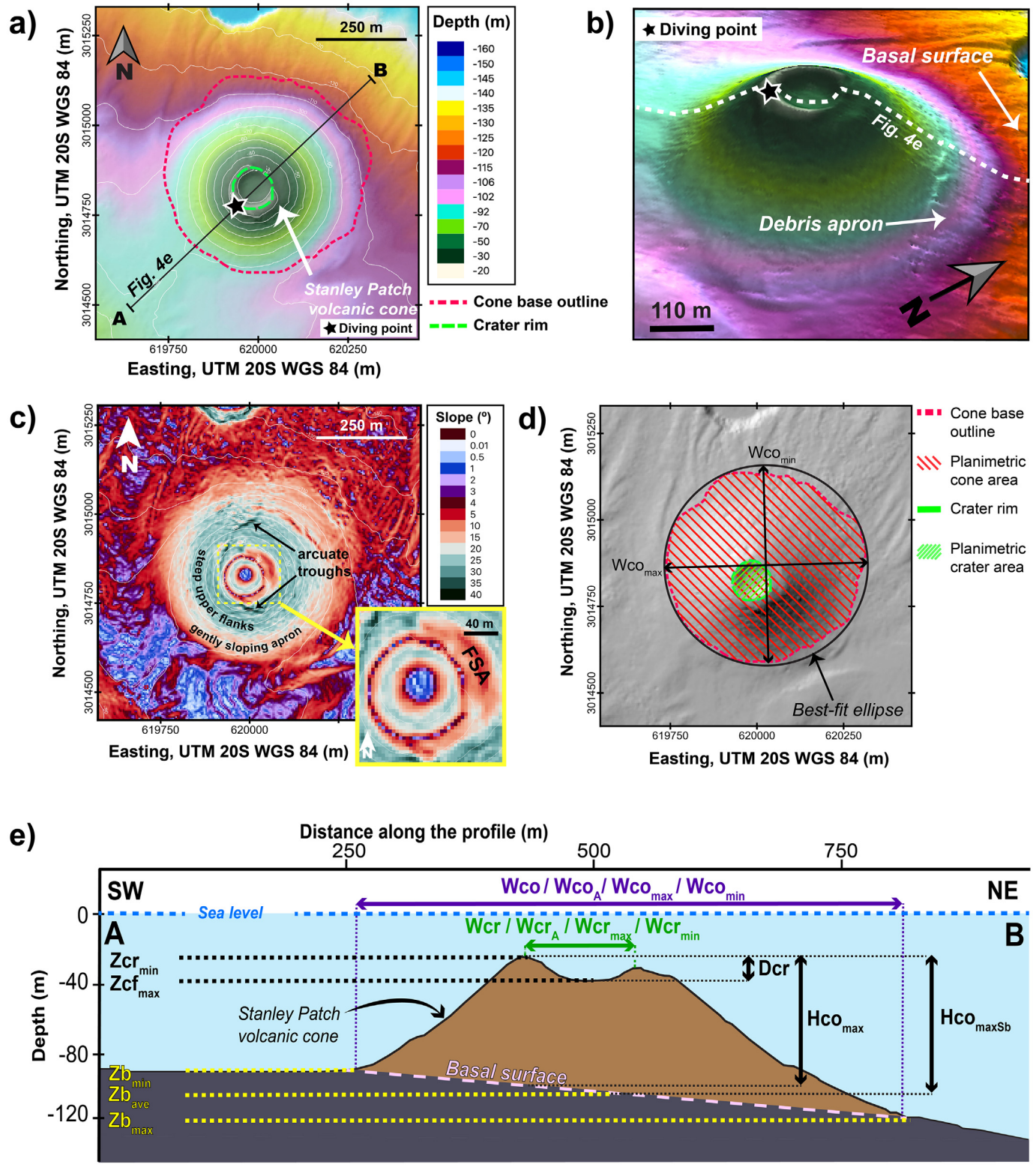

Fig. 4. a) Bathymetric map of Stanley Patch volcano, showing the location of the profiles displayed at e) as well as the cone base outline and crater rim. b) 3D shaded relief map of Stanley Patch volcano: the debris apron around the NE side of the cone are clearly observed. c) Slope map of Stanley Patch volcano, showing the location of the flat summit area (FSA), the arcuate flank troughs and the surrounding debris apron. d) DEM-derived upper view of Stanley Patch volcano. Cone and crater planimetric area, cone base outline and crater rim are also indicated. e) Bathymetric profile across SW-NE direction (see a) and b) for location). The morphological parameters measured at the cone are also indicated (see Table 1 for further explanation) (modified from Angulo-Preckler et al., 2021).

wt% for Si, Al, Na, Mg, Mn, Fe and Ni and below 0.03 wt% for Ca and K. Ti, Cr and Sr show higher detection limits (0.08 wt%, 0.14 wt% and 0.3 wt%, respectively). An up to 20-μm-diameter defocused beam was used for groundmass analyses in order to minimize Na migration.

We also analyzed the stable isotopic ratios (δD, $\delta^{18}O$) of the selected samples. To prepare the samples for analysis we removed several centimeters of material from the surface of each sample to avoid late isotopic modification by weathering. Absence of secondary minerals such as

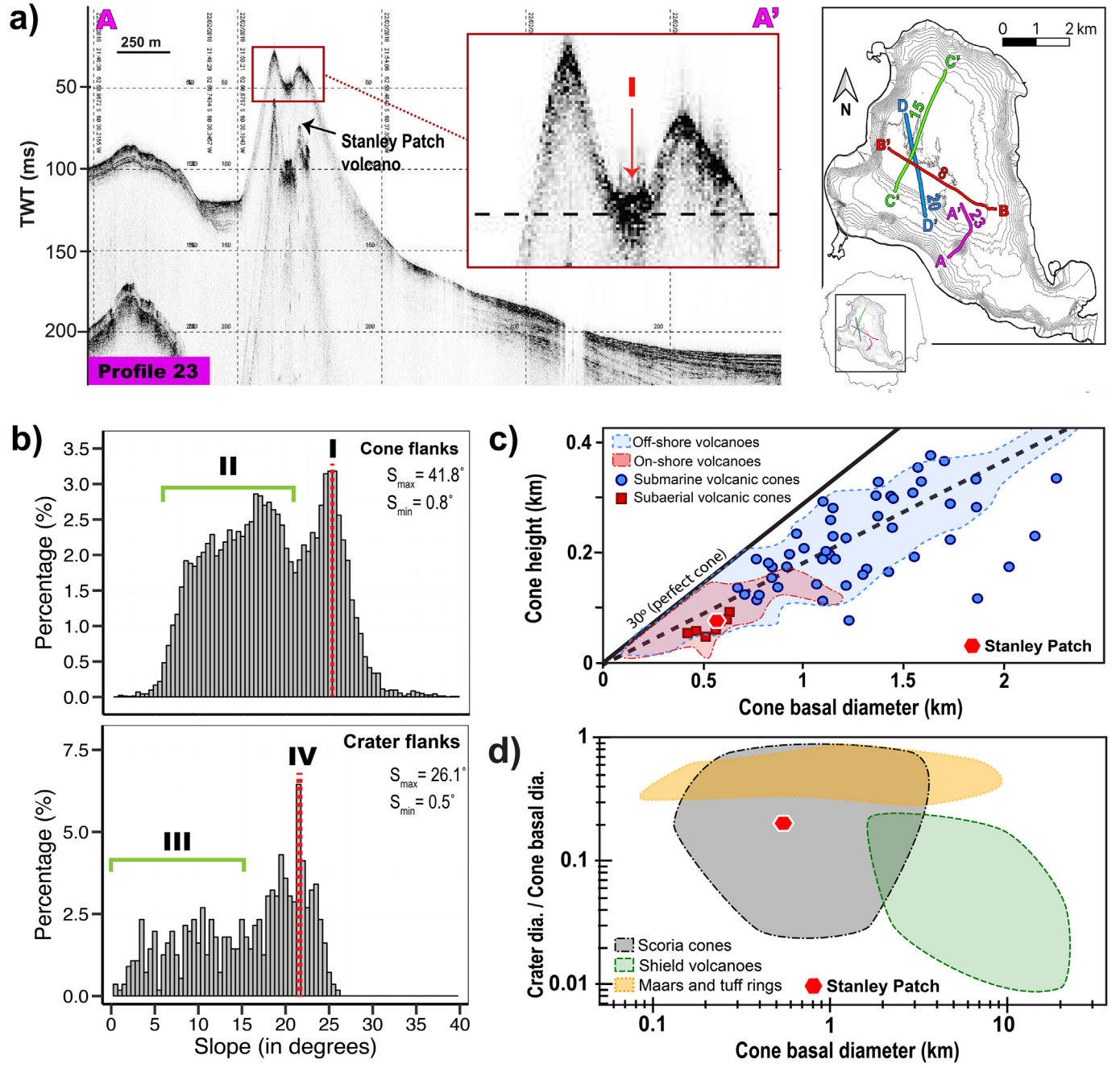

Fig. 5. NW-SE high resolution seismic profiles across Stanley Patch volcano (available at Gómez-Ballesteros et al., 2018). TWT: Two-way-time proxy for depth. The map on the right indicates the location of the profile A - A' (Profile 23) and of those included in Fig. 6a–c. b) Density slope diagrams of the cone (top) and crater inner flanks (bottom). c) Average cone basal diameter vs height for Stanley Patch volcano compared to well-studied on-shore and off-shore volcanic edifices observed at Pico Island (Azores) (blue circles and red squares, data from Mitchell et al., 2012) and Terceira Rift/São Miguel island (blue and red area, data from Weiß et al., 2015). d) Crater diameter/cone basal diameter ratio vs cone basal diameter of Stanley Patch volcano compared to the values for several other types of terrestrial volcanic edifices according to Brož and Hauber (2013).

zeolite group minerals was confirmed through an exhaustive petrographic analysis. The hydrogen and oxygen isotopic analyses were carried out at the Servicio General de Análisis de Isótopos Estables (NUCLEUS - Universidad de Salamanca, https://nucleus.usal.es/en/isotopes) following the detailed extraction procedures, standards and equipment used, as well as reproducibility determination, described in Álvarez-Valero et al. (2020).

Argon isotopic ratios of the groundmass materials already analyzed by XRF in samples SUB_3, SUB_4, and SUB_7 were measured using a noble-gas mass spectrometer MS-IV (a modified VG-5400) in the Department of General Systems Studies, Graduate School of Arts and Sciences, The University of Tokyo. K% is obtained by the K_2O wt% content through the XRF analysis described above. The analytical procedure in detail and calculation method are described by Miyoshi et al. (2012), Mori and Mashima (2005), Nagao et al. (1984, 1996) and Orihashi et al. (2004).

4. Results

4.1. Morphological analysis

Stanley Patch rises sharply from the north-east trending and gently dipping (~3°) seafloor (Figs. 4e and S3). The overall shape of both crater and base is very circular with a planimetric basal (Aco) and crater area (Acr) of ~2.4 × 10^5 m^2 and ~ 0.1 × 10^5 m^2, respectively. The volcanic

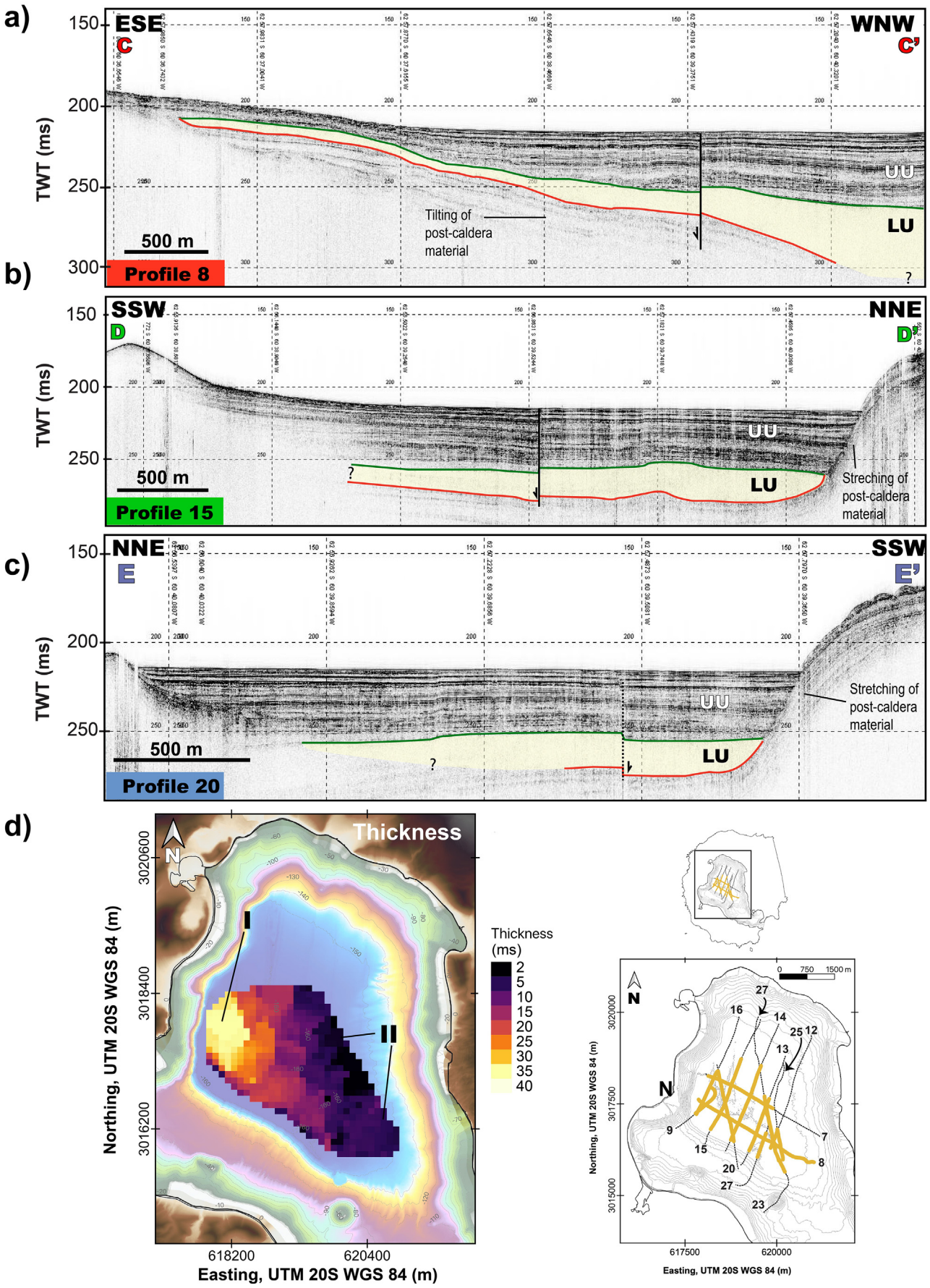
a)
ESE
C
WNW
C'
TWT (ms)
150
200
250
300
500 m
Profile 8
Tilting of post-caldera material
UU
LU
?
b)
SSW
D
NNE
D'
TWT (ms)
500 m
Profile 15
UU
LU
?
Streching of post-caldera material
c)
NNE
E
SSW
E'
TWT (ms)
500 m
Profile 20
UU
LU
?
Stretching of post-caldera material
d)
Thickness
N
I
II
Thickness (ms)
2
5
10
15
20
25
30
35
40
Northing, UTM 20S WGS 84 (m)
3020600
3018400
3016200
618200
620400
Easting, UTM 20S WGS 84 (m)
0 750 1500 m
27
16
14
25
12
13
9
15
20
27
23
7
8
3020000
3017500
3015000
617500
620000
Easting, UTM 20S WGS 84 (m)

cone presents a maximum basal diameter (Wco_{max}) of ~589 m and a minimum diameter (Wco_{min}) of ~578 both obtained from a manually drawn best-fitting ellipse, where the major axis corresponds to the cone's maximum diameter (Wood, 1980b) (Fig. 4d, Table 1). The average cone basal diameter varies from 584 m (Wco) to 553 m (Wco_A) depending if calculated as the arithmetic mean of Wco_{max} and Wco_{min} (i.e., Wco) (e.g., Pedrazzi et al., 2020; Wood, 1980b) or estimated as the diameter of a circle with an area equivalent to Aco (i.e., Wco_A) (e.g., Favalli et al., 2009; Kervyn et al., 2012). Maximum cone height (Hco_{max}) is ~77 m but rises up to ~80 m (Hco_{maxSb}) when considering it as difference between the average basal elevation (Zb_{ave}) and the minimum water depth observed at the cone's rim crest or summit (Zb_{min}) (Table 1 and Fig. 4d) (Settle, 1979). This results in similar height and width ratios regardless of the calculation method, ranging between ~0.132 (Hco_{max}/Wco) and 0.145 (Hco_{maxSb}/Wco_A), and a cone volume (Vco) of 0.06 km^3.

The crater rim has a shallow crest with a maximum (Wcr_{max}) and minimum (Wcr_{min}) diameter of 123 and 117 m, respectively. The average crater diameter ranges from 113 m (Wcr_A) to 120 m (Wcr) depending on the calculation method (Table 1). This results in a Wcr and cone basal diameter ratio in the range of ~0.193 (Wcr_A/Wco) to 0.217 (Wcr/Wco_A). The crater floor is flat with a diameter (Wcf) of ~39 m and a maximum depth (Dcr) of ~13 m (Table 1, Fig. 4d).

The cone is characterized by steep upper flanks, separated by a break-in-slope from a gentle sloping apron (Figs. 4b and c). The cone slope angle histogram shows two major slope angle modes centered at ~25° (Fig. 5b I) and a broad feature between 8 and 20° (Fig. 5b II). The intra-crater slopes are generally less steep (Figs. 4c and 5b III), partially due to the crater floor being filled up by sediments (Fig. 5a I). The Stanley Patch cone is also characterized by the following morphological features (Fig. 4b and c): (1) a flat to gentle sloping wide crest of the crater rim (5–15°) on the northeast side; (2) a break-in-slope between the uniformly inclined flanks and a gentle sloping apron surrounding the Stanley Patch volcano; and (3) two arcuate troughs running from N to S on the flanks.

4.2. Petrographic and geochemical analyses

The rock samples collected on the crater rim of Stanley Patch correspond to low density and poorly vesicular (25–35% vesicles volume; Houghton and Wilson, 1989) scoriaceous fragments from 2 to 15 cm in size (Figs. 2e and S4). Vesicle sizes are normally smaller than 1 mm, rarely reaching up to 3–4 mm, and fairly elongated to irregular in shape. In hand specimens, the fragments are usually black, with local reddish-brown oxidized zones. Most samples show a < 0.5 mm thick, yellow to green carbonate crust corresponding to encrusting coralline algae.

At microscopic scale, the studied samples are porphyritic with phenocrysts content below 1–2 vol% immersed in a hyalopilitic textured groundmass consisting of plagioclase, pyroxene, Fe—Ti oxides, and interstitial glass. Phenocrysts are dominated by euhedral plagioclase crystals from 0.5 to 1.0 mm in diameter, with minor subhedral phenocrysts of clinopyroxene and olivine ranging from 0.3 to 0.5 mm (Figs. 2e and S4). Quenching textures such as skeletal or dendritic shapes are not observed. Spiky crystals with swallow-tailed terminations are scarce, whereas sideromelane is mainly present as micrometric glass fragments filling vesicles.

Based on whole rock geochemistry, the sampled rocks classify as subalkaline basaltic trachyandesites and basaltic andesites (53–55 wt% SiO_2) (Figs. 2c and S6, Table S3). Despite their small range in composition, they present slightly negative correlations of MgO and CaO with SiO_2, and positive ones of K_2O and Na_2O (Fig. S7). REE contents depict nearly straight trends in a chondrite-normalized diagram without significant anomalies (Fig. S8). In contrast, marked positive anomalies (Cs and Pb) and negative (Nb) anomalies occur in the primitive-mantle normalized diagram (Fig. S9).

Olivine micropheno- and microcrystals show forsterite contents ranging from Fo_{49} to Fo_{72} and Ni contents varying from 33 to 563 ppm. Microphenocrysts and phenocrysts of pyroxenes (augites), show composition of $Wo_{25–44}$, $En_{37–52}$, $Fs_{10–22}$. Plagioclases are mainly labradorites and andesines with An_{62} – An_{38} (Fig. S10c and Table S7). In sample SUB_7, plagioclase ranges from bytownite to oligoclase (An_{75} to An_{10}). In addition, samples SUB_4 and SUB_7 display local ilmenite and titano-magnetite (Fig. S10d and Table S8). Glass compositions are notably variable, going from basaltic to trachyandesitic with SiO_2 contents of 51–59 wt% and 56–62 wt% in samples SUB_5, SUB_7, and SUB_8, respectively (Fig. S6). In contrast, regarding silica content, glass is mostly homogeneous in samples SUB_3 and SUB_4. In general, glasses show a negative correlation of MgO and CaO with SiO_2, and a positive correlation of K_2O and Na_2O. Contents of TiO_2, FeOt, Al_2O_3, and MnO show a notable chemical dispersion (Figs. S6 and S7). This significant variation in the compositional ranges of phenocrystals and glasses is consistent with the mixing mechanisms occurring at depth, which are widely observed in the products of the entire island (e.g. Smellie, 2001, 2002a; Geyer et al., 2019, 2021).

D/H ratios of the Stanley Patch samples range from −58.4 to −99.5‰ (Fig. S11) with homogeneous water contents of 0.1–0.2 wt% (Table S9). All samples fall within the range of regular primary magmatic fluids (i.e., igneous waters in Fig. S11), slightly above and immediately below the isotopic composition of N-MORB mantle (−60‰; Clog et al., 2013). $\delta^{18}O$ values show small variation from 5.0 to 6.3‰ within the usual values of basaltic rocks on Earth (≈ 3.5–7‰) (Bindeman, 2008), and in line with the onland samples of the island (Álvarez-Valero et al., 2020).

4.3. Shallow seismic sub-bottom structure of Port Foster

The ultra-high resolution seismic stratigraphy of the uppermost (< 300 ms) deposits infilling Port Foster (Figs. 6 and S1) show two distinct sedimentary units abutting the monoclinal structure. The Lower Unit (LU) represents a striking and relatively thick seismically transparent body that occupies an extensive part of sub-basin 1, onlapping its margins (Figs. 6 and S1). This unit reaches its maximum thickness of ~38 ms (i.e., ~ 30–36 m) in the northwest, at the base of (or even beneath) the western submerged flank of Wensleydale Beacon's volcanic edifice (Fig. 6d I); it gets thinner towards the north and north-east of the bay (Fig. 6d II). The volume of this unit is estimated to be >0.055 km^3. The LU, which correlates to sub-unit C1 of Rey et al. (1995, 1997) (Figs. 3d and e) and Kowalewski et al. (1990), is overlaid by an Upper Unit (UU) (up to c. 50 ms thick). The UU, equivalent to sub-unit C2 of Rey et al. (1995, 1997) and C2 plus D of Kowalewski et al. (1990), is made up of the vertically stacked even-layered deposits separated by irregular transparent bodies (a few ms thick), which resemble smaller-scale mass-flow deposits (Fig. 6).

5. Discussion

5.1. Stanley Patch: a submerged subaerial volcanic cone

The height and width ratios for the edifice and its crater show an overlap with terrestrial scoria cones (e.g., Kervyn et al., 2012; Settle,

Fig. 6. (a) to (c) Seismic profiles obtained within Port Foster (available at Gómez-Ballesteros et al., 2018). See Fig. 5a for location. The Lower Unit (LU) is colored in yellow with its top and base highlighted in green and red, respectively. If clearly visible, faults are also indicated. UU: Upper Unit. See text for further details. d) Thickness map (in ms) estimated for the Lower Unit. The orange colour indicates the lateral coverage where the Lower Unit is observable in the seismic profile included in a) to c) and in Figs. 5a and S1.

Table 1
Morphometric parameters measured for Stanley Patch volcano. b.s.l. Below sea level.

Parameter	Unit	Description	Value
Aco	m^2	Planimetric area of the cone including crater and outer flanks (see Fig. 4d).	$2.4 \cdot 10^5$
Acr	m^2	Planimetric area of the cone crater including crater floor and inner flanks (see Fig. 4d).	$1 \cdot 10^4$
Dcr	m	Crater depth calculated as (Hooper and Sheridan, 1998; Wood, 1980a): $Dcr = Zcf_{max} - Zcr_{min}$	13
Hco_{max}	m	Maximum cone height calculated as the maximum elevation of the crater rim above the 3D basal surface (see Fig. 3e) (Favalli et al., 2009).	77
Hco_{maxSb}	m	Maximum cone height calculated as Settle (1979): $Hco_{maxSb} = Zb_{ave} - Zcr_{min}$	80
Sb_{mean}	degree	Slope of the basal plane obtained by applying a linear regression to the points obtained along a profile aligned along the maximum dip direction of the basal surface (Fig. S3c and g).	3
Vco	km^3	Cone volume enclosed between the DEM surface and the 3D base surface determined from the surrounding topography and the bilinear/bicubic spline interpolation with Tykhonov regularization (see Fig. S3e).	0.06
Wcr_{max}	m	Maximum crater diameter measured along four profiles spaced 45° azimuthally, with one of them aligned along the maximum dip direction of the basal surface (Wood, 1980b)	123
Wcr_{min}	m	Minimum crater diameter measured along four profiles spaced 45° azimuthally, with one of them aligned along the maximum dip direction of the basal surface (Wood, 1980b)	117
Wcr	m	Average crater diameter calculated as (Wood, 1980b): $Wcr = (Wcr_{max} + Wcr_{min})/2$	120
Wcr_A	m	Average crater diameter calculated as (Favalli et al., 2009): $Wcr_A = (4 \cdot Acr/\pi)^{0.5}$	113
Wco_{max}	m	Maximum cone basal diameter obtained from a manually drawn best-fitting ellipse, where the major axis corresponds to the cone's maximum diameter (Wood, 1980b) (see Fig. 4d).	589
Wco_{min}	m	Maximum cone basal diameter obtained from a manually drawn best-fitting ellipse, where the major axis corresponds to the cone's maximum diameter (Wood, 1980b) (see Fig. 4d).	578
Wco	m	Average cone basal diameter calculated as (Wood, 1980b): $Wco = (Wco_{max} + Wco_{min})/2$	584
Wco_A	m	Average cone basal diameter calculated as (Favalli et al., 2009): $Wco_A = (4 \cdot Aco/\pi)^{0.5}$	553
Zb_{max}	m	Maximum basal depth b.s.l. (in absolute value).	120
Zb_{min}	m	Minimum basal depth b.s.l. (in absolute value).	90
Zb_{ave}	m	Average basal depth b.s.l. (in absolute value) calculated as: $Zb_{ave} = (Zb_{max} - Zb_{min})/2$	105
Zcf_{max}	m	Maximum depth b.s.l. (in absolute value) of the cone crater floor.	38
Zcr_{min}	m	Minimum depth b.s.l. (in absolute value) of the cone crater rim.	25

1979; Wood, 1980b) (e.g., Fig. 5d). The obtained values, independent of the calculation method applied, match with young cone populations from Mt. Etna (Italy) (Favalli et al., 2009), Lanzarote (Canary Island) (Kervyn et al., 2012), and Mauna Kea (Hawaii) (Kervyn et al., 2012). The morphometric values of Stanley Patch, however, are in contrast with onshore monogenetic edifices, which are mostly tuff cones and tuff rings with much wider craters and lower edifice height/width ratios (Pedrazzi et al., 2020). In general, submarine pyroclastic cone populations show a much larger range of edifice height and width ratios, and typically they are larger in volume (Fig. 5c) (e.g., Mitchell et al., 2012; Weiß et al., 2015).

The bimodal slope angle distribution of the cone flanks (Fig. 5b I and II) can correspond to hillslope erosion and sediment transport. The gentle sloping areas around the cone (Fig. 4b and c) are interpreted to be a debris apron formed due to *syn*-eruptive reworking and post-eruptive erosional processes (e.g. debris flows) (e.g., Dohrenwend et al., 1986; Ferrucci et al., 2005; Kereszturi and Németh, 2016a; McGetchin et al., 1974). The steeper (~ 25°) upper cone flanks have a slope angle lower than the typical angle of repose value (30–35°) (Wood, 1980a, 1980b), indicating eruption-related deviation of the pyroclastic successions, including grain size, welding, and agglutination differences among flank sectors (e.g., Kereszturi et al., 2012; Kereszturi and Németh, 2016b; Kervyn et al., 2012; Valentine et al., 2005), and/or erosional processes (e.g., Hooper and Sheridan, 1998). The arcuate troughs on the flank of Stanley Patch resemble discontinuity surfaces and small-stepped scars due to partial cone collapse (Fig. 4c). These features are present at many unwelded scoria cones (e.g., Németh et al., 2011; Riggs and Duffield, 2008; Sumner, 1998), and also observed in analogue experiments (Grosse et al., 2012). The geomorphology of the crater rim also suggests erosional rounding (e.g., Pelletier and Cline, 2007). The lower intra crater wall slope angles are interpreted to be caused by erosional modification, suggesting a post-eruptive rim-to-crater sediment transport combined with marine sedimentation.

Quenching of basaltic magma by surface water commonly forms a rim of pale brown glass (sideromelane) that progressively grades inward into more crystalline black glass (tachylite). Tachylite is the product of slower cooling rates, which yield a glass groundmass that hosts abundant cryptocrystalline microlites and/or nanolites of opaque mineral phases, commonly Fe—Ti oxides (e.g., White et al., 2015). In addition, it also typically produces quenching textures in crystals, such as skeletal, dendritic, or globular shapes. On the other hand, interaction of magma with external water may enhance fragmentation either by hydromagmatic processes (which may also occur in subaerial settings) or hyaloclastite formation (exclusive from underwater conditions). In addition, it is widely accepted that magma-water interaction also affects the shape and volume of the vesicles (e.g. Mastin et al., 2004; Stovall et al., 2011; Ross and White, 2012). After emplacement, under wet and hot conditions, sideromelane quickly alters into palagonite (Stroncik and Schmincke, 2002). These key features of magma-water interactions are absent in the Stanley Patch samples, thus supporting negligible magma-water contact during the eruption (e.g., Bryan, 1972; Jercinovic et al., 1990; Walton and Schiffman, 2003).

Direct contact between seawater and magma -or volcanic rocks- during eruption or cooling can modify the original δD ratios of the glass towards heavier values (e.g., Friedman et al., 1993). δD ratios (in the range of −58.4 to −99.5‰) and water contents (0.1–0.2 wt%) of the studied samples are consistent with an initial magma composition within the range of the N-MORB mantle ($\delta D = -60 \pm 5‰$; Clog et al., 2013). and show no significant isotope contribution from seawater into the studied rocks. Thus, δD ratios and water contents preclude significant magma-seawater interaction during eruption or cooling, further supporting the subaerial origin of Stanley Patch.

Therefore, we state that the results of the morphological analysis, supported by the petrographic and isotopic geochemical data from the collected rock samples, suggest a subaerial origin for Stanley Patch despite its current subaqueous location.

5.2. Dating of Stanley Patch volcano

The numerous analytical and technical limitations of the K—Ar dating method makes it inapplicable for samples younger than 2000 years (e.g., Miyoshi et al., 2012; Mori and Mashima, 2005; Nagao et al., 1984; Nagao et al., 1996; Nier, 1950; Orihashi et al., 2004; Schaeffer and Zähringer, 1966; Solé, 2009). However, it is a useful age constraint test for the upper age limit of the Stanley Patch volcano. The $^{40}Ar/^{36}Ar$ ratios of the glasses (Table S9) are lower than the atmospheric $^{40}Ar/^{36}Ar$

(296.0) ratio. This yields negative $^{40}Ar^*$ (non-atmospheric ^{40}Ar) values that in turn imply negative K—Ar ages, i.e., less than 2000 years. Consequently, considering the subaerial origin of Stanley Patch cone and the proposed ages for its formation, the complete flooding of Port Foster by seawater likely happened during the last 2000 years. This agrees with the age of the caldera collapse of 3980 ± 125 calibrated years BP based on tephrochronology, sedimentology studies and ^{14}C dates (Antoniades et al., 2018) as well as the fact that the volcanic edifice is built on top of over a ~ 100 ms thick pile of post-caldera sediments (at least, sub-units B1 to B3) (Rey et al., 1995, 1997, 2002; Somoza et al., 2004), suggesting a considerable time period between the caldera collapse and the Stanley Patch's formation (Fig. 3d).

5.3. Reconstructing the past history of Deception Island's caldera

Our results support the hypothesis that Stanley Patch volcano grew in a subaerial environment, hence indicating that at least the southern (shallower) sector of Port Foster (i.e., sub-basins 2 and 3) was not covered by water immediately after the caldera collapse. This reveals that the complete flooding of Deception Island caldera by seawater could only have occurred after the formation of Stanley Patch volcano. This, combined with the previously published stratigraphic, sedimentological, geophysical and petrological data, allows us to depict a comprehensive geologic evolution of Deception Island. We distinguish the following major evolutionary stages and events: (i) pre-caldera stage; (ii) caldera collapse event; (iii) early (pre-flooding) post-caldera stage; (iv) caldera sea flooding event; and (v) late (post-flooding) post-caldera stage (Fig. 7).

5.3.1. Pre-caldera stage

Most of the pre-caldera volcanic activity likely originated from several vents, representing a period of shoaling and emergence of the volcanic island (Fig. 7a) (e.g., Baker et al., 1975; Baraldo et al., 2003; Birkenmajer, 1992; Hawkes, 1961; Holtedahl, 1929; Martí and Baraldo, 1990; Olsacher, 1956; Smellie, 2001, 2002a). The most recent paleo-topographic reconstruction of the island suggests the presence of a paleo-edifice with a paleo-summit height of about 640 m.a.s.l and parasitic volcanoes (<< 650 m height) in the locations presently known as Neptunes Bellows and Macaroni Point (Fig. 7a) (Torrecillas et al., 2013).

5.3.2. Caldera collapse event

During the caldera collapse, the OCTF was emplaced radially from the caldera borders, mantling older deposits and progressively infilling the caldera depression (e.g., Martí et al., 2013; Smellie, 2001, 2002a). Most probably, the caldera collapse took place through distinct caldera blocks that subsided (likely synchronous) into the emptying magma chamber (e.g., Martí et al., 2013) (Fig. 7b). In this sense, the fault-related monocline currently separating the bay's sub-basins may represent the limit of -at least- two subsiding blocks (Fig. 7b). The caldera collapse can therefore be subdivided into a central zone (main block, current sub-basin 1) and a marginal zone tilted towards the caldera interior (secondary block(s), current sub-basins 2 and 3). Subsidence difference between the two main described blocks at the moment of the caldera collapse is still uncertain. However, the current deformation, stretching and tilting of the post-caldera sedimentary units observed in the seismic profiles (Unit B in Figs. 3d, e and 6) indicate that the main block has been continuously subsiding in a trap-door manner since the caldera collapse (Rey et al., 2002). This collapse mechanism and structure is similar to other calderas worldwide (e.g., Rotorua, New Zealand; Milner et al., 2002) and consistent with the modelling results of sand-box analogues (e.g., Acocella, 2006, 2007; Geyer et al., 2006; Roche and Druitt, 2001). Considering the figures presented by Martí et al. (2013) based on available geophysical data (e.g., Ben-Zvi et al., 2009; Grad et al., 1992; Luzón et al., 2011; Rey et al., 1995; Zandomeneghi et al., 2009), the caldera floor may have subsided ~1.8 km, whereas the intra-caldera OCTF deposits would be as thick as ~1.2 km (Fig. 7b). Based on our present findings, the secondary block, corresponding to sub-basins 2 and 3, should have stayed "dry" at least until the construction of Stanley Patch volcano (< ~ 2000 years ago). The caldera should have remained closed to the sea and, most probably, was only filled by fresh water coming from rainfall, and snow and ice melting, which accumulated in the deepest parts of the northern sub-block or sub-basin 1 (Fig. 7b and c). During decades and even centuries after the collapse, the water level of this shallow lake may have varied as seen in other caldera systems potentially hosting internal lacustrine ecosystems (e.g., Sete Cidades-Azores; Rull et al., 2017; Vázquez-Loureiro et al., 2019).

5.3.3. Early (pre-flooding) post-caldera stage

After the caldera-forming event, volcanic activity was characterized by (e.g., Smellie, 2001, 2002a): (i) the formation of scoria cones aligned along previous active fissures (Fig. 7c I); (ii) abundant effusive activity on the outer slopes leading to prominent lava platforms (Fig. 7c II); (iii) occasional lava flows within the caldera (Fig. 7c III) and over the caldera wall (Fig. 7c IV); and (iv) hydromagmatic activity from centers distributed both outside (e.g., Baily Head (Fig. 7c V)) and within the caldera (Fig. 7c VI). During this period, volcanic activity also occurred inside the bay in sub-basins 2 and 3 as previously interpreted from the seismic profiles across Port Foster and as evidenced by the presence of Stanley Patch volcano (Fig. 7c VII).

5.3.4. Caldera sea flooding event

At some time after the formation of Stanley Patch volcano, the caldera became open to the sea leading to its complete flooding. Our ultra-high resolution seismic stratigraphy of the uppermost (< 300 ms) deposits infilling Port Foster (see Figs. 6 and S1), in line with the observations made by Kowalewski et al. (1990), indicates a sharp change in the sedimentary history of the bay after the deposition of the LU. The shape, seismic facies, boundaries and thickness distribution of this unit, all point to a large mass-flow deposit (e.g., Casas et al., 2013; Masson et al., 1996) sourced from the southeast (Whalers Bay and/or Neptunes Bellows area) (Fig. 7d I). The seismic characteristics of the LU displayed by the ultra-high resolution TOPAS profiles show transparent facies resembling an amalgamated deposit with local lack of penetration of the acoustic signal. An irregular blocky character with hyperbolic echoes is not observed. The LU has been previously interpreted as the result of the sudden deposition of pyroclastic materials carried down by large onshore-generated lahars (Kowalewski et al., 1990). However, since it is the thickest and most voluminous sedimentary unit compared to the ones composing the UU, we state that it originated due to an extreme and unique event, not since repeated. We propose that the LU corresponds to the materials deposited by an exceptional mass flow event that occurred during the outburst flood that inundated the caldera to its present sea level. Here, we use the term mass flow as a generic expression that involves different types of sediment-gravity flows, e.g., debris flow, debris avalanches. Nevertheless, those processes on volcanic environments are not distinct and/or separate but may be part of a process continuum (Mulder and Cochonat, 1996; Masson et al., 1998). Likewise, the distribution of the slide sediment is in general governed by the nature of the landslide material, the flow process and/or the emplacement speed (e.g., Masson et al., 2002). Both considerations would imply that the process responsible of the LU could have initiated as a debris avalanches evolving to a debris flow due to disaggregation occurred during the transport that extends to the interior of Port Foster. Similar processes have been considered to occur in the Canary Islands (e.g., Masson et al., 1998). We have not evidences/information about the mechanical behaviour of the slope failure at the headwall/source area, only evidences of the distal domain (depositional) of that sediment gravity-driven event. A mass flow event that in any case is unique in the area based on its magnitude, as it is well reflected by the stratigraphic divisions and their deposits.

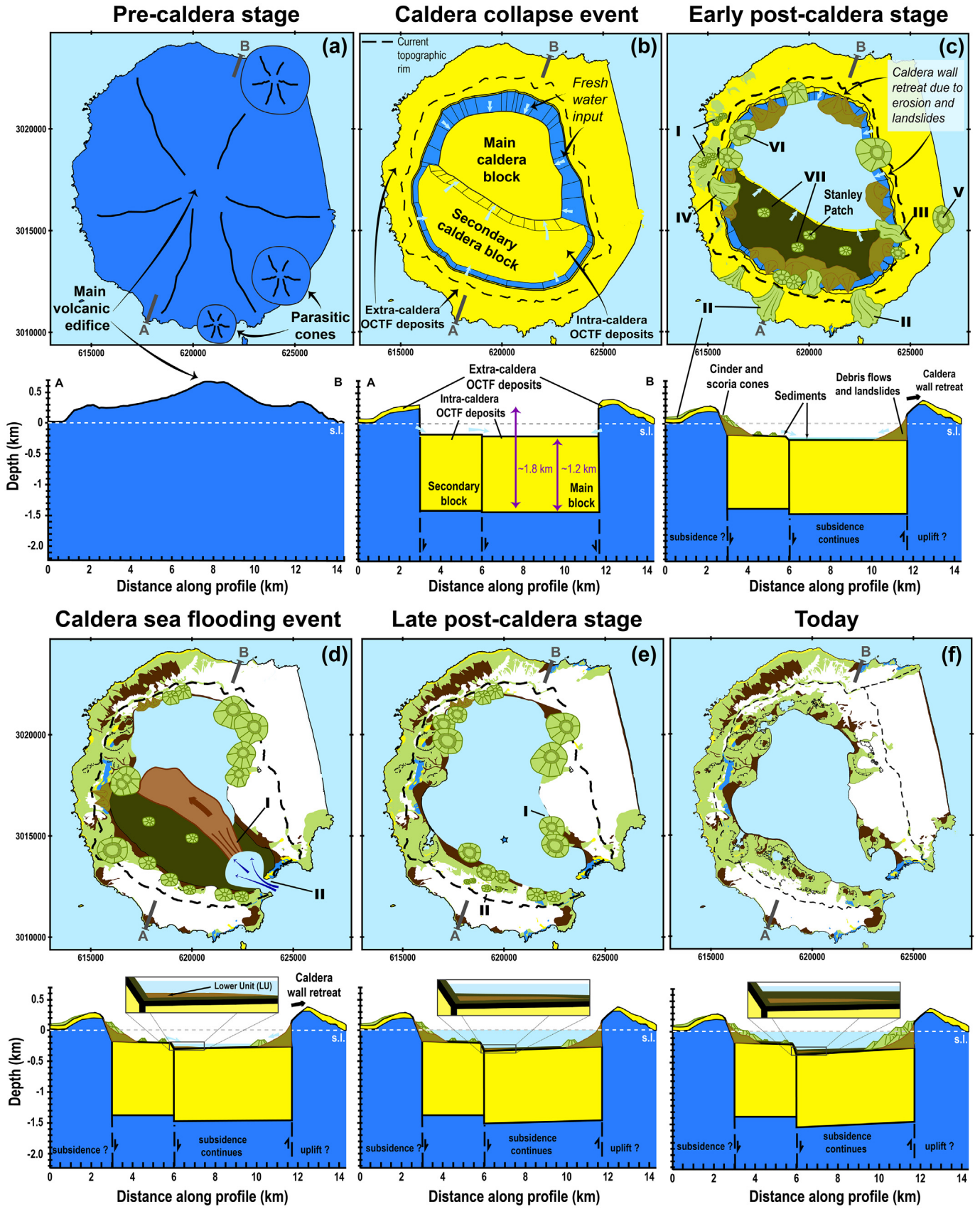

Fig. 7. Conceptual model of the evolution of Deception Island based on the review of available geological and geophysical data and new results presented in this work. Main phases and events include: a) pre-caldera stage; b) caldera-forming event; c) early post-caldera phase; d) caldera flooding event; e) post-flooding phase; and f) current stage. Legend as per Fig. 2a.

Accounting with all the sedimentological and morphological features of the LU pointing its source at the southeast of the bay, and the fact that the volume of this body (> 0.055 km^3) can be roughly correlated with the "missing" material from Neptunes Bellows (Figs. 8a and b). We conclude that it resulted from the sudden collapse of the caldera wall at that precise location. This opened the inner area of the island -at that time below sea level- to the ocean (Fig. 7d I). This argument agrees with the stratigraphic observations by Kowalewski

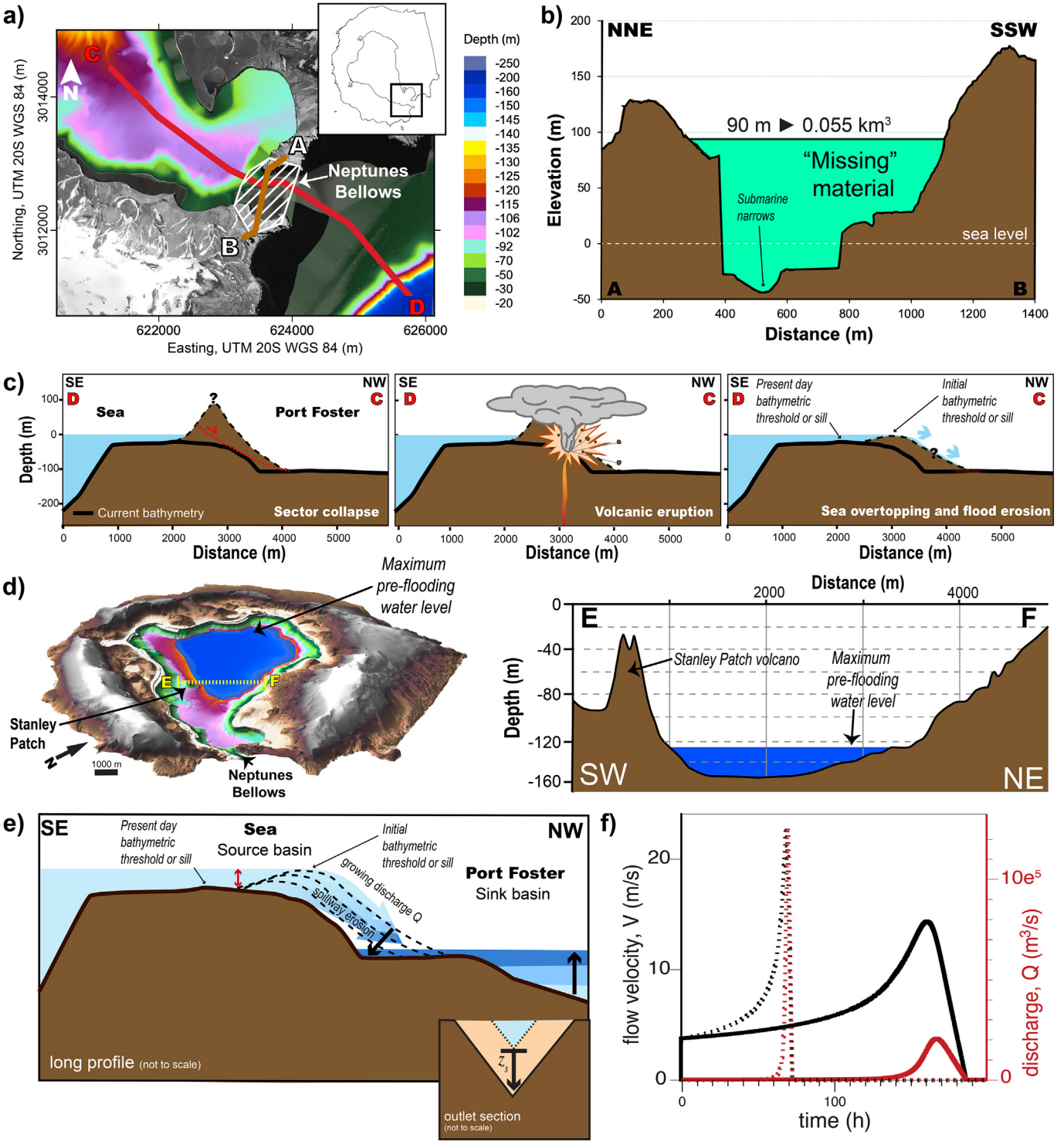

Fig. 8. DEM of Port Foster and orthophotomap of Deception Island showing in plan view (white dashed area) and cross sectional view (green colored area in b) of the area used to estimate the volume "missing" from Neptunes Bellows; c) Sketch of the three different, yet not mutually exclusive processes, that may have led to the opening of the caldera to the sea and consequently, to the outburst flood. d) 3D shaded relief map of Deception Island (left) and bathymetric profile of Port Foster (right). The maximum pre-flooding water level is indicated. Vertical exaggeration: ×1.5. e) Conceptual model (section along the inlet) of sea overtopping and outburst flood development as a result of water discharge and inlet erosion at the threshold. For the parameters involved see the text. f) Numerical model results of flood development after breaching or overtopping. Curves for water velocity *V* (in black) and discharge Q (in red) are shown for two final sill depths (final depth of the threshold below sea level): 15 m (solid lines) and 30 m (dashed lines). See main text and Fig. S13 for further details.

et al. (1990), who concluded that the flooding of the caldera by seawater may have occurred after the deposition of their unit B (our LU), and that C and D (composing our UU) were undoubtedly deposited in submarine conditions.

5.3.5. Late (post-flooding) post-caldera stage

After the flooding, volcanic activity continued on the island until historical times and as recently as 1970, around the shores of Port Foster (Fig. 7e I), and along on-land fissures (Fig. 7e II). Since the caldera flooding episode, the volcanic activity in the deepest parts of Port Foster has been apparently limited to hydrothermal venting with no clear evidence of submarine or Surtseyan activity (Somoza et al., 2004). The shallow seismic sub-bottom stratigraphy and facies of the UU point to a significant change in the sedimentation of Port Foster, as it is suggested by the unconformity dividing the UU of the LU, and the distinctive expression of UU seismic facies.

5.4. Estimating the timing of the outburst flood and caldera refilling

Three main, yet not mutually exclusive, processes may have initiated the caldera wall breach and hence, triggered a sea flooding event (Fig. 8c): (i) a flank instability and major collapse of the pre-caldera edifice to the open sea or the caldera interior (e.g., Acosta et al., 1992); (ii) the occurrence of an explosive eruption at the caldera wall (e.g., Aparicio et al., 1997; Baraldo and Rinaldi, 2000); or (iii) overtopping of the sea potentially facilitated by the weakening of the caldera wall due to water infiltration leading to minor collapses. Once the oceanic water overtops the caldera wall, the erosion caused by the water influx gradually (but with initial rates increasing potentially; Figs. 8e and S13) enlarges and deepens the spillway (e.g., Kataoka, 2011). Among these three scenarios, the overtopping is the most conservative in terms of flood duration and peak discharge, because it assumes that the initial inflow of water is small and only its own erosion contributes to enlarge the inlet, thus progressively increasing the inflow rate. The smooth U-shape of the seaway floor and the seeming retrogressive erosion suggested by its bathymetry (the submarine bathymetric sill lays today out of the island) (Figs. 8c and d) argues for the third of these mechanisms, by similarity with other scenarios where the overtopping mechanism is well determined (e.g., Lake Bonneville, Abril-Hernández et al., 2018). Assuming this mechanism followed by ever-increasing water erosion of the topographic barrier separating the bay from the ocean, we can estimate a minimum peak water inflow and filling time (Fig. 8d). The mechanism is similar to other floods taking place due to the overtopping of lakes (O'Connor et al., 2013). However, in our case, contrary to floods sourced at natural lakes or breaching artificial dams, the water source (upper reservoir: the ocean) was effectively infinite. Hence, the flooding is limited by the size of the sink (the lower reservoir: the caldera), which is filled up to sea level.

To estimate the timing of the caldera refilling by overtopping of the sea at the Neptunes Bellows, we assume that: i) Port Foster was empty up to, at least, the base of the Stanley volcano, which remained exposed in an endorheic evaporitic basin at a depth below sea level similar to today's (i.e., 90–120 m b.s.l.) (Fig. 8d); (ii) the present depth of Neptunes Bellows has not been modified by subsidence of the island or eustatic sea level changes; and iii) the present depth of the submarine bathymetric threshold between the caldera and the open ocean (30 m b.s.l.) is at least partially related to the erosion produced during the refilling flood (Figs. 8c and d). The latter is supported by the absence of comparable sea level changes since the formation of Stanley Patch volcano (Hallmann et al., 2018). Post-volcanic subsidence (of a tectonic or thermal nature) of the threshold area (or of the entire island), may undermine this assumption.

We use the present depth of the bathymetric threshold or sill (30 m; Figs. 8c and S12) as a constraint on the erosion produced during refilling, and apply a coupled erosion/hydrodynamic model to estimate the progress of the refill (Garcia-Castellanos and O'Connor, 2018). The numerical model spillover (available at https://github.com/danigeos/spillover) iteratively calculates the water discharge across a certain threshold as a function of its depth below a source water body (the global ocean in our scenario), and for a lower basin (sink) of known area and depth (Fig. 8e). This is coupled to a progressive deepening of the threshold due to erosion exerted by the water flow, following a basal shear-stress power law (Howard and Kerby, 1983).

$$\frac{dz_s}{dt} = -k_e \tau^a \quad (1)$$

where $z_s(t)$ is the depth of the sill (Fig. 8e), t is time, k_e is the erodibility of the rock, and τ is the shear stress at the base of the flow, proportional to water velocity, with an $a = 1.5$ (See Garcia-Castellanos and O'Connor (2018) for a detailed formulation). For the calculation of basal shear stress and water velocity we adopt a critical flow at the sill where overtopping takes place and a sill widening that is proportional to its depth. We adjust the width's linear dependence on depth such as to fit the final model's width to the present observed width of the submarine narrows (120 m; Figs. 8b and S12).

With the aim of showing the sensitivity of the flood evolution to the total cumulative erosion at the inlet, results in Fig. S13 show two floods calculated for an initial one-meter deep breach of the ocean into the caldera, reaching a final erosion depth of 15 and 30 m, respectively. These two scenarios aim to show the sensitivity of our results to the assumption that most of this depth originated during the refill process. The rock erodibilities required for both scenarios are $k_e = 1.8e^{-3}$ m yr^{-1} Pa$^{-1.5}$ and $4.2e^{-3}$ m yr^{-1} Pa$^{-1.5}$; these values are consistent with the relatively weak volcanic lithology of the barrier, considering that linking erodibility to lithology involved orders of magnitude of uncertainty (Garcia-Castellanos and O'Connor, 2018). Increasing the initial breach depth only advances the timing of the flood and vice versa, while keeping the peak discharge values largely unchanged. In the first scenario, the basin (Port Foster) is refilled in 180 h, although most of the flow is concentrated in the last 40 h. The second scenario evolves faster due to the weaker barrier and the refill takes place in only 100 h, with 95% of the flow concentrated in the last 10 h. Peak discharge changes from $1.92 \cdot 10^4$ to $1.24 \cdot 10^5$ m^3 s^{-1}. Erosion rates (Fig. S13) reach values 15 times faster in the second scenario. Thus, the first scenario, causing an erosion of only half of the present depth of the threshold, represents an estimation of the slowest refill mechanisms considered in this work. We can therefore conclude that, if most of the present depth of the threshold is related to erosion during the refill rather than to eustatic changes, then the process was very rapid, in the form of an outburst flood lasting a few days or less. Our results indicate that the filling of Deception Island's empty basin, only 3.5 km^3 in volume, may have proceeded to completion at peak rates of at least thousands of m^3 s^{-1}, thus completing the bulk of the flooding in a time period of a few days or less (Figs. 8f and S13). This is comparable in order of magnitude to the estimates by Nomikou et al. (2016), the ~20 km^3 Santorini caldera was filled in <2 days, involving a water velocity larger than 19 m/s and a water discharge above $2.5 \cdot 10^5$ m^3 s^{-1}.

6. Summary and conclusions

Significant efforts have been made to understand the complex magmatic and volcanic evolution of Deception Island. However, very few studies exist about the submerged volcanic edifices within Port Foster. The new geophysical data (bathymetric data and ultra-high resolution parametric seismic profiles of Port Foster) obtained during the 2017–2018 Spanish Antarctic Campaign, and the juvenile rock samples collected from Stanley Patch by SCUBA diving have allowed shedding new light on the eruptive event that lead to the formation of the largest volcanic edifice within Port Foster. The morphological characterization of this volcanic edifice, and the petrographic description and chemical analyses of the collected rock samples, all point to a subaerial

monogenetic explosive eruption as responsible for the formation of this scoria cone. This reveals that the caldera could have opened to the sea leading to its complete flooding only after the construction of Stanley Patch volcano (< ~ 2000 years ago). The caldera wall breach could have been triggered by a sector collapse of the pre-caldera edifice, the occurrence of an explosive eruption and/or overtopping of the sea with gradual erosion of the spillway. Anyhow, Deception Island's empty basin, may have been completely flooded in a few days or less, leading to an important inflexion point in the island's geological evolution. The flooding event not only changed the sedimentary dynamics within the caldera depression, but it also changed the eruptive style of post-caldera volcanic activity incrementing the potential of phreatomagmatic eruptions. This highlights the complex temporal and spatial aspects of a changing hazard landscape that must be incorporated into any volcanic hazard assessment of volcanic islands.

Data availability

Bathymetric data supporting this research, obtained by the Spanish Marine Hydrographic Institute, belong to the Ministry of Defense of Spain and are restricted to the public due to security reasons.

Seismic profiles for this research are available in Gómez-Ballesteros et al. (2018). Seismic Profiles from Port Foster, Deception Island (Antarctica). SEANOE. doi:10.17882/77208

Declaration of Competing Interest

The authors declare that they have no known competing financial interests or personal relationships that could have appeared to influence the work reported in this paper.

Acknowledgments

This research was supported by the Spanish Government RECALDEC (CTM2009-05919-E/ANT), PEVOLDEC (CTM2011-13578-E/ANT), POSVOLDEC (CTM2016-79617-P)(AEI/FEDER, UE), VOLGASDEC (PGC2018-095693-B-I00), USAL-2019 project (Programa Propio - mod. 1B) and the GALIEO-IHM Program. A.G. is grateful for her Ramón y Cajal contract (RYC-2012-11024), and A.M.A-V for the grant under the "JSPS invitation fellowship" program (S18113). D.P. is grateful for his Beatriu de Pinós (2016 BP 00086) and Juan de la Cierva (IJCI-2016-30482) contracts. We thank all the military staff of the Spanish Antarctic Base "Gabriel de Castilla", BIO Hespérides oceanographic cruise and the Marine Hydrographic Institute, for their constant help and logistic support. This research is part of POLARCSIC and PTI VOLCAN activities. English editing by Grant George Buffett (www.terranova.barcelona). We thank the Editor, J.L. Macías, and both reviewers A. Di Roberto and P. Nomikou for their constructive comments that have allowed improving a previous version of this manuscript.

Appendix A. Supplementary data

Supplementary data to this article can be found online at https://doi.org/10.1016/j.jvolgeores.2021.107249.

References

Abril-Hernández, J.M., Periáñez, R., O'Connor, J.E., Garcia-Castellanos, D., 2018. Computational fluid dynamics simulations of the late Pleistocene Lake Bonneville Flood. J. Hydrol. 561, 1–15. https://doi.org/10.1016/j.jhydrol.2018.03.065.

Acocella, V., 2006. Caldera types: how end-members relate to evolutionary stages of collapse. Geophys. Res. Lett. 33, L18314. https://doi.org/10.1029/2006GL027434.

Acocella, V., 2007. Understanding caldera structure and development: an overview of analogue models compared to natural calderas. Earth Sci. Rev. 85, 125–160. https://doi.org/10.1016/j.earscirev.2007.08.004.

Acosta, J., Herranz, P., Sanz, J.L., Uchipi, 1992. Antarctic continental margin: geologic image of the Bransfield Trough, an incipient oceanic basin. In: Poag, W.E., De Graciansky, P.E. (Eds.), Geologic Evolution of Atlantic Continental Rises. Van Nostrand Reinhold, London, pp. 49–61.

Agusto, M., Caselli, A.T., Poma, S.U., 2007. Estudio volcanológico del sector occidental de la Isla Decepción (Antártida): caracterización geoquímica y análisis evolutivo. Rev. Asoc. Geol. Argent. 62, 530–544.

Almendros, J., Carmona, E., Jiménez, V., Díaz-Moreno, A., Lorenzo, F., Berrocoso, M., de Gil, A., Fernandez-Ros, A., Rosado, B., 2015. Deception Island (Antarctica): sustained deformation and large increase in seismic activity during 2014-2015. Bull. Glob. Volcanism Netw. 40 (6).

Almendros, J., Carmona, E., Jiménez, V., Díaz-Moreno, A., Lorenzo, F., 2018. Volcano-Tectonic activity at Deception Island Volcano following a Seismic Swarm in the Bransfield Rift (2014–2015). Geophys. Res. Lett. 45 (10), 4788–4798. https://doi.org/10.1029/2018gl077490.

Álvarez-Valero, A.M., Gisbert, G., Aulinas, M., Geyer, A., Kereszturi, G., Polo-Sánchez, A., Núñez-Guerrero, E., Sumino, H., Borrajo, J., 2020. δD and δ18O variations of the magmatic system beneath Deception Island volcano (Antarctica): implications for magma ascent and eruption forecasting. Chem. Geol. 542. https://doi.org/10.1016/j.chemgeo.2020.119595.

Angulo-Preckler, C., Pernet, P., García-Hernández, C., Kereszturi, G., Álvarez-Valero, A.M., Hopfenblatt, J., et al., 2021. Volcanism and rapid sedimentation affect the benthic communities of Deception Island, Antarctica. Cont. Shelf Res. 104404. https://doi.org/10.1016/j.csr.2021.104404.

Antoniades, D., Giralt, S., Geyer, A., Álvarez-Valero, A.M., Pla-Rabes, S., Granados, I., Liu, E.J., Toro, M., Smellie, J.L., Oliva, Marc, 2018. The timing and widespread effects of the largest Holocene volcanic eruption in Antarctica. Sci. Rep. 8 (1), 17279. https://doi.org/10.1038/s41598-018-35460-x.

Aparicio, A., Menegatti, N., Petrinovic, I., Risso, C., Viramonte, J.G., 1997. El volcanismo de Isla Decepción (Península Antártida). Bol. Geol. Min. 108 (3), 19–42.

Baker, P.E., 1969. Investigations of the 1967 and 1969 volcanic eruptions on Deception Island, South Shetland Islands. Polar Rec. 14 (93), 823–827. https://doi.org/10.1017/S003224740006544X.

Baker, P.E., McReath, I., 1971. 1970 volcanic eruption at Deception Island. Nat. Phys. Sci. 231 (3), 5–9. https://doi.org/10.1038/physci231005a0.

Baker, P.E., Davies, T.G., Roobol, M.J., 1969. Volcanic activity at Deception Island in 1967 and 1969. Nature 224 (5219), 553–560. https://doi.org/10.1038/224553a0.

Baker, P.E., McReath, I., Harvey, M.R., Roobol, M.J., Davies, T.G., 1975. The geology of the south Shetland islands: volcanic evolution of Deception island. British Antarctic Survey Scientific Reports. Vol. 78 81 pp.

Baraldo, A., Rinaldi, C.A., 2000. Stratigraphy and structure of Deception Island, South Shetland Islands, Antarctica. J. S. Am. Earth Sci. 13 (8), 785–796. https://doi.org/10.1016/S0895-9811(00)00060-2.

Baraldo, A., Rapalini, A.E., Böhnel, H., Mena, M., 2003. Paleomagnetic study of Deception Island, South Shetland Islands, Antarctica. Geophys. J. Int. 153 (2), 333–343. https://doi.org/10.1046/j.1365-246X.2003.01881.x.

Barclay, A.H., Wilcock, W.S.D., Ibáñez, J.M., 2009. Bathymetric constraints on the tectonic and volcanic evolution of Deception Island Volcano, South Shetland Islands. Antarct. Sci. 21 (2), 153–167. https://doi.org/10.1017/S0954102008001673.

Barker, P.F., 1982. The Cenozoic subduction history of the Pacific margin of the Antarctic Peninsula: ridge crest–trench interactions. J. Geol. Soc. 139 (6), 787–801. https://doi.org/10.1144/gsjgs.139.6.0787.

Bartolini, S., Geyer, A., Martí, J., Pedrazzi, D., Aguirre-Díaz, G., 2014. Volcanic hazard on Deception Island (South Shetland Islands, Antarctica). J. Volcanol. Geotherm. Res. 285, 150–168. https://doi.org/10.1016/j.jvolgeores.2014.08.009.

Bender, N.A., Crosbie, K., Lynch, H.J., 2016. Patterns of tourism in the Antarctic Peninsula region: a 20-year analysis. Antarct. Sci. 28 (3), 194–203. https://doi.org/10.1017/S0954102016000031.

Ben-Zvi, T., Wilcock, W.S.D., Barclay, A.H., Zandomeneghi, D., Ibáñez, J.M., Almendros, J., 2009. The P-wave velocity structure of Deception Island, Antarctica, from two-dimensional seismic tomography. J. Volcanol. Geotherm. Res. 180 (1), 67–80. https://doi.org/10.1016/j.jvolgeores.2008.11.020.

Berrocoso, M., Prates, G., Fernández-Ros, A., Peci, L.M., de Gil, A., Rosado, B., Páez, R., Jigena, B., 2018. Caldera unrest detected with seawater temperature anomalies at Deception Island, Antarctic Peninsula. Bull. Volcanol. 80 (4), 41. https://doi.org/10.1007/s00445-018-1216-2.

Bindeman, I., 2008. Oxygen isotopes in mantle and crustal magmas as revealed by single crystal analysis. Rev. Mineral. Geochem. 69 (1), 445–478. https://doi.org/10.2138/rmg.2008.69.12.

Birkenmajer, K., 1992. Evolution of the Bransfield Basin and rift, West Antarctica. In: Yoshida, Y., Kaminuma, K., Shiraishi, K. (Eds.), Recent Progress in Antarctic Earth Sciences. Terra Scientific Publishing Company, Tokyo, pp. 405–410.

Birkenmajer, K., Soliani, E., Kawashita, K., 1990. Reliability of potassium-argon dating of Cretaceous-Tertiary island-arc volcanic suites of King George Island, South Shetland Islands (West Antarctica). Zbl. Geol. Paläontol. 1, 127–140.

British Antarctic Survey, 1987. Report for 1986/1987. Swindon, Natural Environment Research Council.

Brož, P., Hauber, E., 2013. Hydrovolcanic tuff rings and cones as indicators for phreatomagmatic explosive eruptions on Mars. J. Geophys. Res. E Planets 118 (8), 1656–1675. https://doi.org/10.1002/jgre.20120.

Bryan, W.B., 1972. Morphology of quench crystals in submarine basalts. J. Geophys. Res. (1896–1977) 77 (29), 5812–5819. https://doi.org/10.1029/JB077i029p05812.

Casas, D., Ercilla, G., García, M., Yenes, M., Estrada, F., 2013. Post-rift sedimentary evolution of the Gebra Debris Valley. A submarine slope failure system in the Central Bransfield Basin (Antarctica). Mar. Geol. 340, 16–29. https://doi.org/10.1016/j.margeo.2013.04.011.

Catalán, M., Galindo-Zaldivar, J., Davila, J.M., Martos, Y.M., Maldonado, A., Gambôa, L., Schreider, A.A., 2013. Initial stages of oceanic spreading in the Bransfield Rift from

magnetic and gravity data analysis. Tectonophysics 585, 102–112. https://doi.org/10.1016/j.tecto.2012.09.016.
Catalán, M., Martos, Y.M., Galindo-Zaldívar, J., Funaki, M., 2014. Monitoring the evolution of Deception Island volcano from magnetic anomaly data (South Shetland Islands, Antarctica). Glob. Planet. Chang. 123 (Part), 199–212. https://doi.org/10.1016/j.gloplacha.2014.07.018.
Clog, M., Aubaud, C., Cartigny, P., Dosso, L., 2013. The hydrogen isotopic composition and water content of southern Pacific MORB: a reassessment of the D/H ratio of the depleted mantle reservoir. Earth Planet. Sci. Lett. 381, 156–165. https://doi.org/10.1016/j.epsl.2013.08.043.
Cooper, A.P.R., Smellie, J.L., Maylin, J., 1998. Evidence for shallowing and uplift from bathymetric records of Deception Island, Antarctica. Antarct. Sci. 10 (4), 455–461. https://doi.org/10.1017/S0954102098000558.
De Rosa, R., Mazzuoli, R., Omarini, R., Ventura, G., Viramonte, J., 1995. A volcanological model for the historical eruptions at Deception Island, Bransfield Strait, Antarctica. Terra Antartica 2, 95–101.
Dohrenwend, J.C., Wells, S.G., Turrin, B.D., 1986. Degradation of Quaternary cinder cones in the Cima volcanic field, Mojave Desert, California. Geol. Soc. Am. Bull. 97 (4), 421–427. https://doi.org/10.1130/0016-7606(1986)97<421:DOQCCI>2.0.CO;2.
Fathi, E., Maleki Shoja, B., 2018. Chapter 9 - Deep neural networks for natural language processing. In: Gudivada, V.N., C. R. B. T.-H. of S. Rao (Eds.), Computational Analysis and Understanding of Natural Languages: Principles, Methods and Applications. Vol. 38. Elsevier, pp. 229–316. https://doi.org/10.1016/bs.host.2018.07.006.
Favalli, M., Karatson, D., Mazzarini, F., Pareschi, M.T., Boschi, E., 2009. Morphometry of scoria cones located on a volcano flank: a case study from Mt. Etna (Italy), based on high-resolution LiDAR data. J. Volcanol. Geotherm. Res. 186 (3–4), 320–330. https://doi.org/10.1016/j.jvolgeores.2009.07.011.
Fernandez-Ros, A.M., Berrocoso, M., Ramirez, M.E., 2007. Volcanic deformation models for Deception Island (South Shetland Islands, Antarctica). In: Cooper, A.K., Raymond, C.R. (Eds.), Proceedings of the 10th ISAES (p. Extended Abstract 094) USGS Open File 2007-1047.
Ferrucci, M., Pertusati, S., Sulpizio, R., Zanchetta, G., Pareschi, M.T., Santacroce, R., 2005. Volcaniclastic debris flows at La Fossa Volcano (Vulcano Island, southern Italy): insights for erosion behaviour of loose pyroclastic material on steep slopes. J. Volcanol. Geotherm. Res. 145 (3–4), 173–191. https://doi.org/10.1016/j.jvolgeores.2005.01.013.
Friedman, I., Gleason, J., Sheppard, R.A., Gude, A.J., 1993. Deuterium Fractionation as Water Diffuses into Silicic Volcanic Ash. American Geophysical Union (AGU), pp. 321–323 https://doi.org/10.1029/gm078p0321.
Galé, C., Ubide, T., Lago, M., Gil-Imaz, A., Gil-Peña, I., Galindo-Zaldívar, J., Rey, J., Maestro, A., López-Martínez, J., 2014. Vulcanismo cuaternario de la Isla Decepción (Antártida): una signatura relacionada con la subducción de la Fosa de las Shetland del Sur en el dominio de tras-arco de la Cuenca de Bransfield. Bol. Geol. Min. 125 (1), 31–52.
Garcia-Castellanos, D., O'Connor, J.E., 2018. Outburst floods provide erodability estimates consistent with long-term landscape evolution. Sci. Rep. 8 (1), 1–9. https://doi.org/10.1038/s41598-018-28981-y.
Geyer, A., 2021. Chapter 1.4 Antarctic volcanism: active volcanism overview. Geological Society, London, Memoirs, 55, M55-2020-12 https://doi.org/10.1144/M55-2020-12.
Geyer, A., Folch, A., Martí, J., 2006. Relationship between caldera collapse and magma chamber withdrawal: an experimental approach. J. Volcanol. Geotherm. Res. 157 (4), 375–386. https://doi.org/10.1016/j.jvolgeores.2006.05.001.
Geyer, A., Marti, A., Giralt, S., Folch, A., 2017. Potential ash impact from Antarctic volcanoes: insights from Deception Island's most recent eruption. Sci. Rep. 7 (1). https://doi.org/10.1038/s41598-017-16630-9.
Geyer, A., Álvarez-Valero, A.M., Gisbert, G., Aulinas, M., Hernández-Barreña, D., Lobo, A., Marti, J., 2019. Deciphering the evolution of Deception Island's magmatic system. Sci. Rep. 9 (1), 373. https://doi.org/10.1038/s41598-018-36188-4.
Geyer, A., Pedrazzi, D., Almendros, J., Berrocoso, M., López-Martínez, J., Maestro, A., et al., 2021. Chapter 7.1 Deception Island. Geological Society, London, Memoirs, 55, M55-2018-56 https://doi.org/10.1144/M55-2018-56.
Gómez-Ballesteros, et al., 2018. Seismic Profiles from Port Foster, Deception Island (Antarctica). SEANOE https://doi.org/10.17882/77208.
González-Ferrán, O., Katsui, Y., 1970. Estudio integral del volcanismo cenozoico superior de las Islas Shetland del Sur, Antartica. Ser. Cient. Inst. Antart. Chileno 22 (2), 123–174.
González-Ferrán, O., Munizaga, F., Moreno, R., H., 1971. 1970 eruption at Deception island: distribution and chemical features of ejected materials. Antarct. J. US 6 (4), 87–89.
Grad, M., Guterch, A., Sroda, P., 1992. Upper crustal structure of Deception Island area, Bransfield Strait, West Antarctica. Antarct. Sci. 4 (4), 469–476. https://doi.org/10.1017/S0954102092000683.
Grosse, P., van Wyk de Vries, B., Euillades, P.A., Kervyn, M., Petrinovic, I.A., 2012. Systematic morphometric characterization of volcanic edifices using digital elevation models. Geomorphology 136 (1), 114–131. https://doi.org/10.1016/j.geomorph.2011.06.001.
Haase, K.M., Beier, C., Fretzdorff, S., Smellie, J.L., Garbe-Schönberg, D., 2012. Magmatic evolution of the South Shetland Islands, Antarctica, and implications for continental crust formation. Contrib. Mineral. Petrol. 163 (6), 1103–1119. https://doi.org/10.1007/s00410-012-0719-7.
Hallmann, N., Camoin, G., Eisenhauer, A., Botella, A., Milne, G.A., Vella, C., Samankassou, E., Pothin, V., Dussouillez, P., Fleury, J., Fietzke, J., 2018. Ice volume and climate changes from a 6000 year sea-level record in French Polynesia. Nat. Commun. 9 (1), 285. https://doi.org/10.1038/s41467-017-02695-7.
Hamilton, E.L., 1970. Sound velocity and related properties of marine sediments, North Pacific. J. Geophys. Res. (1896–1977) 75 (23), 4423–4446. https://doi.org/10.1029/JB075i023p04423.
Hawkes, D.D., 1961. The geology of the South Shetland Islands: II. The geology and petrology of Deception Island. Falkland Islands Dependencies Survey Scientific Reports. Vol. 27, p. 43.
Hole, M.J., Saunders, A.D., Rogers, G., Sykes, M.A., 1994. The relationship between alkaline magmatism, lithospheric extension and slab window formation along continental destructive plate margins. Geol. Soc. Lond., Spec. Publ. 81 (1). https://doi.org/10.1144/GSL.SP.1994.081.01.15 265.
Holtedahl, O., 1929. On the geology and physiography of some Antarctic and sub-Antarctic islands. Scientific Results of the Norwegian Antarctic Expedition. Vol. 3.
Hooper, D.M., Sheridan, M.F., 1998. Computer-simulation models of scoria cone degradation. J. Volcanol. Geotherm. Res. 83 (3–4), 241–267. https://doi.org/10.1016/S0377-0273(98)00031-6.
Houghton, B.F., Wilson, C.J.N., 1989. A vesicularity index for pyroclastic deposits. Bull. Volcanol. 51, 451–462. https://doi.org/10.1007/bf01078811.
Howard, A.D., Kerby, G., 1983. Channel changes in badlands. GSA Bull. 94 (6), 739–752. https://doi.org/10.1130/0016-7606(1983)94<739:ccib>2.0.co;2.
Ibáñez, J.M., Almendros, J., Carmona, E., Martínez-Arévalo, C., Abril, M., 2003a. The recent seismo-volcanic activity at Deception Island volcano. Deep-Sea Res. II Top. Stud. Oceanogr. 50 (10−11), 1611–1629. https://doi.org/10.1016/S0967-0645(03)00082-1.
Ibáñez, J.M., Carmona, E., Almendros, J., Saccorotti, G., Del Pezzo, E., Abril, M., Ortiz, R., 2003b. The 1998–1999 seismic series at Deception Island volcano, Antarctica. J. Volcanol. Geotherm. Res. 128 (1), 65–88. https://doi.org/10.1016/S0377-0273(03)00247-6.
Jercinovic, M.J., Keil, K., Smith, M.R., Schmitt, R.A., 1990. Alteration of basaltic glasses from north-Central British Columbia, Canada. Geochim. Cosmochim. Acta 54 (10), 2679–2696. https://doi.org/10.1016/0016-7037(90)90004-5.
Johnston, E.N., Sparks, R.S.J., Nomikou, P., Livanos, I., Carey, S., Phillips, J.C., Sigurdsson, H., 2015. Stratigraphic relations of Santorini's intracaldera fill and implications for the rate of post-caldera volcanism. J. Geol. Soc. 172, 323–335. https://doi.org/10.1144/jgs2013-114.
Kataoka, K.S., 2011. Geomorphic and sedimentary evidence of a gigantic outburst flood from Towada caldera after the 15ka Towada-Hachinohe ignimbrite eruption, Northeast Japan. Geomorphology 125 (1), 11–26. https://doi.org/10.1016/j.geomorph.2010.08.006.
Keller, R.A., Fisk, M.R., White, W.M., Birkenmajer, K., 1992. Isotopic and trace element constraints on mixing and melting models of marginal basin volcanism, Bransfield Strait, Antarctica. Earth Planet. Sci. Lett. 111 (2), 287–303. https://doi.org/10.1016/0012-821X(92)90185-X.
Kereszturi, G., Németh, K., 2016a. Post-eruptive sediment transport and surface processes on unvegetated volcanic hillslopes – a case study of Black Tank scoria cone, Cima Volcanic Field, California. Geomorphology 267, 59–75. https://doi.org/10.1016/j.geomorph.2016.05.023.
Kereszturi, G., Németh, K., 2016b. Sedimentology, eruptive mechanism and facies architecture of basaltic scoria cones from the Auckland Volcanic Field (New Zealand). J. Volcanol. Geotherm. Res. 324, 41–56. https://doi.org/10.1016/j.jvolgeores.2016.05.012.
Kereszturi, G., Jordan, G., Nemeth, K., Doniz-Pérez, J., 2012. Syn-eruptive morphometric variability of monogenetic scoria cones. Bull. Volcanol. 74 (9), 2171–2185. https://doi.org/10.1007/s00445-012-0658-1.
Kervyn, M., Ernst, G.G.J., Carracedo, J.C., Jacobs, P., 2012. Geomorphometric variability of "monogenetic" volcanic cones: evidence from Mauna Kea, Lanzarote and experimental cones. Geomorphology 136 (1), 59–75. https://doi.org/10.1016/j.geomorph.2011.04.009.
Kowalewski, W., Rudowski, S., Zalewski, S.M., 1990. Seismoacoustic studies within flooded part of the caldera of the Deception Island, West Antarctica. Pol. Polar Res. 11 (3–4), 259–266.
Le Bas, M.J., Le Maitre, R.W., Streckeisen, A., Zanettin, B., Rocks, I. S. on the S. of I, 1986. A chemical classification of volcanic rocks based on the total alkali-silica diagram. J. Petrol. 27 (3), 745–750. https://doi.org/10.1093/petrology/27.3.745.
López-Martínez, J., Serrano, E., 2002. Geomorphology. In: López-Martínez, J., Smellie, J.L., Thomson, J.W., Thomson, M.R.A. (Eds.), Geology and Geomorphology of Deception Island. British Antarctic Survey, Cambridge, Cambridge, pp. 31–39.
López-Martínez, J., Serrano, E., Rey, J., Smellie, J.L., 2000. Geomorphological map of Deception Island. Sheet 6B. In: López-Martínez, J., Smellie, J.L., Thomson, J.W., Thomson, M.R.A. (Eds.), Geology and Geomorphology of Deception Island. British Antarctic Survey, Cambridge Cambridge, BAS GEOMAP Series, Sheets 6-A and 6-B, 1:25 000.
Luzón, F., Almendros, J., García-Jerez, A., 2011. Shallow structure of Deception Island, Antarctica, from correlations of ambient seismic noise on a set of dense seismic arrays. Geophys. J. Int. 185 (2), 737–748. https://doi.org/10.1111/j.1365-246X.2011.04962.x.
Martí, J., Baraldo, A., 1990. Pre-caldera pyroclastic deposits of Deception Island (South Shetland Islands). Antarct. Sci. 2 (4), 345–352. https://doi.org/10.1017/S0954102090000475.
Martí, J., Vila, J., Rey, J., 1996. Deception Island (Bransfield Strait, Antarctica): an example of a volcanic caldera developed by extensional tectonics. Geol. Soc. Spec. Publ., 253–265 https://doi.org/10.1144/GSL.SP.1996.110.01.20.
Martí, J., Geyer, A., Aguirre-Diaz, G., 2013. Origin and evolution of the Deception Island caldera (South Shetland Islands, Antarctica). Bull. Volcanol. 75 (6), 1–18. https://doi.org/10.1007/s00445-013-0732-3.
Masson, D.G., Kenyon, N.H., Weaver, P.P.E., 1996. Slides, debris flows, and turbidity currents. In: Summerhayes, C.P., Thorpe, R.S. (Eds.), Oceanography: An Illustrated Guide. Manson Publishing, London, pp. 136–151.
Masson, Canals, Alonso, Urgeles, Huhnerbach, 1998. The Canary Debris Flow: source area morphology and failure mechanisms. Sedimentology 45, 411–432. https://doi.org/10.1046/j.1365-3091.1998.0165f.x.

Masson, D.G., Watts, A.B., Gee, M.J.R., Urgeles, R., Mitchell, N.C., Le Bas, T.P., Canals, M., 2002. Slope failures on the flanks of the western Canary Islands. Earth Sci. Rev. 57 (1–2), 1–35. https://doi.org/10.1016/S0012-8252(01)00069-1.

Mastin, L.G., Christiansen, R.L., Thornber, C., Lowenstern, J., Beeson, M., 2004. What makes hydromagmatic eruptions violent? Some insights from the Keanakāko'i Ash, Kīlauea Volcano, Hawai'i. J. Volcanol. Geotherm. Res. 137 (1), 15–31. https://doi.org/10.1016/j.jvolgeores.2004.05.015.

McCarron, J.J., Larter, R.D., 1998. Late cretaceous to early Tertiary subduction history of the Antarctic Peninsula. J. Geol. Soc. 155 (2), 255–268. https://doi.org/10.1144/gsjgs.155.2.0255.

McGetchin, T.R., Settle, M., Chouet, B.A., 1974. Cinder cone growth modeled after Northeast Crater, Mount Etna, Sicily. J. Geophys. Res. 79 (23), 3257–3272. https://doi.org/10.1029/JB079i023p03257.

Middlemost, E.A.K., 1989. Iron oxidation ratios, norms and the classification of volcanic rocks. Chem. Geol. 77, 19–26. https://doi.org/10.1016/0009-2541(89)90011-9.

Milner, D.M., Cole, J.W., Wood, C.P., 2002. Asymmetric, multiple-block collapse at Rotorua Caldera, Taupo Volcanic Zone, New Zealand. Bull. Volcanol. 64 (2), 134–149. https://doi.org/10.1007/s00445-001-0191-0.

Mitchell, N.C., Stretch, R., Oppenheimer, C., Kay, D., Beier, C., 2012. Cone morphologies associated with shallow marine eruptions: East Pico Island, Azores. Bull. Volcanol. 74 (10), 2289–2301. https://doi.org/10.1007/s00445-012-0662-5.

Miyoshi, M., Sumino, H., Miyabuchi, Y., Shinmura, T., Mori, Y., Hasenaka, T., et al., 2012. K-Ar ages determined for post-caldera volcanic products from Aso volcano, Central Kyushu, Japan. J. Volcanol. Geotherm. Res. 229–230, 64–73. https://doi.org/10.1016/j.jvolgeores.2012.04.003.

Mori, Y., Mashima, H., 2005. X-ray fluorescence analysis of major and trace elements in silicate rocks using 1:5 dilution glass beads. Bull. Kitakyushu Mus. Nat. Hist. Hum. Hist. Ser. A (Nat. Hist.) 3, 1–12.

Mulder, T., Cochonat, P., 1996. Classification of offshore mass movements. J. Sediment. Res. 66 (1), 43–57. https://doi.org/10.1306/D42682AC-2B26-11D7-8648000102C1865D.

Nagao, K., Nishido, H., Itaya, T., Ogata, K., 1984. An age determination by K–Ar method. Bull. Hiruzen Res. Inst. 9, 19–38.

Nagao, Keisuke, Ogata, A., Miura, Y.N., Yamaguchi, K., 1996. Ar isotope analysis for K-Ar dating using two modified-VG5400 mass spectrometers-I: Isotope dilution method. J. Mass Spectrom. Soc. Jpn. 44 (1), 39–61. https://doi.org/10.5702/massspec.44.39.

Németh, K., Risso, C., Nullo, F., Kereszturi, G., 2011. The role of collapsing and cone rafting on eruption style changes and final cone morphology: Los Morados scoria cone, Mendoza, Argentina. Cent. Eur. J. Geosci. 3 (2), 102–118. https://doi.org/10.2478/s13533-011-0008-4.

Nier, A.O., 1950. A redetermination of the relative abundances of the isotopes of carbon, nitrogen, oxygen, argon, and potassium. Phys. Rev. 77 (6), 789–793. https://doi.org/10.1103/PhysRev.77.789.

Nomikou, P., Druitt, T.H., Hübscher, C., Mather, T.A., Paulatto, M., Kalnins, L.M., Kelfoun, K., Papanikolaou, D., Bejelou, K., Lampridou, D., Pyle, D.M., Carey, S., Watts, A.B., Weiß, B., Parks, M.M., 2016. Post-eruptive flooding of Santorini caldera and implications for tsunami generation. Nat. Commun. 7. https://doi.org/10.1038/ncomms13332.

O'Connor, J.E., Clague, J.J., Walder, J.S., Manville, V., Beebee, R.A., 2013. 9.25 Outburst Floods. Treatise in Geomorphology. Academic Press, San Diego, pp. 475–510 https://doi.org/10.1016/B978-0-12-374739-6.00251-7.

Oliva-Urcia, B., Gil-Peña, I., Maestro, A., López-Martínez, J., Galindo-Zaldívar, J., Soto, R., Gil-Imaz, A., Rey, J., Pueyo, O., 2015. Paleomagnetism from Deception Island (South Shetlands archipelago, Antarctica), new insights into the interpretation of the volcanic evolution using a geomagnetic model. Int. J. Earth Sci., 1–18 https://doi.org/10.1007/s00531-015-1254-3.

Olsacher, J., 1956. Contribucion a la geologia de la Antartida Occidental, I. Contribucion al conocimiento geologico de la Isla Decepcion. Vol. 2. Instituto Antártico Argentino Publicaciones, pp. 19–76.

Orheim, O., 1972. A 200-Year Record of Glacier Mass Balance at Deception Island, Southwest Atlantic Ocean, and its Bearing on Models of Global Climate Change. Vol. 42. Institute of Polar Studies, Ohio State University 118 pp.

Orihashi, Y., Naranjo, J.A., Motoki, A., Sumino, H., Hirata, D., Anma, R., Nagao, K., 2004. Quaternary volcanic activity of Hudson and Lautaro volcanoes, Chilean Patagonia: new constraints from K-Ar ages. Rev. Geol. Chile 31 (2), 207–224. https://doi.org/10.4067/S0716-02082004000200002.

Paredes, C., Pérez-López, R., Giner-Robles, J.L., Martínez-Dí-az, J.J., de la Vega, R., De Vicente, S., Queral, C., Gonzalez-Casado, J.M., 2006. Stochastic three-dimensional conditioned distribution of faults potentially responsible for the seismo-volcanic activity in Deception Island (South Shetland - Antarctica): VISHNU Project. Terra Antartica Rep. 12, 133–144.

Pedrazzi, D., Aguirre-Díaz, G., Bartolini, S., Martí, J., Geyer, A., 2014. The 1970 eruption on Deception Island (Antarctica): eruptive dynamics and implications for volcanic hazards. J. Geol. Soc. 171 (6), 765–778. https://doi.org/10.1144/jgs2014-015.

Pedrazzi, D., Németh, K., Geyer, A., Álvarez-Valero, A.M., Aguirre-Díaz, G., Bartolini, S., 2018. Historic hydrovolcanism at Deception Island (Antarctica): implications for eruption hazards. Bull. Volcanol. 80 (1), 11. https://doi.org/10.1007/s00445-017-1186-9.

Pedrazzi, D., Kereszturi, G., Lobo, A., Geyer, A., Calle, J., 2020. Geomorphology of the post-caldera monogenetic volcanoes at Deception Island, Antarctica – implications for landform recognition and volcanic hazard assessment. J. Volcanol. Geotherm. Res. 402. https://doi.org/10.1016/j.jvolgeores.2020.106986.

Pelletier, J.D., Cline, M.L., 2007. Nonlinear slope-dependent sediment transport in cinder cone evolution. Geology 35 (12), 1067–1070. https://doi.org/10.1130/G23992A.1.

R Core Team, 2014. R: A Language and Environment for Statistical Computing. R Foundation for Statistical Computing, Vienna, Austria URL. http://www.R-project.org/.

Rey, J., Somoza, L., Martínez-Frías, J., 1995. Tectonic, volcanic, and hydrothermal event sequence on Deception Island (Antarctica). Geo-Mar. Lett. 15 (1), 1–8. https://doi.org/10.1007/bf01204491.

Rey, J., Somoza, L., Martínez-Frías, J., Benito, R., Martín-Alfageme, S., 1997. Deception Island (Antarctica): a new target for exploration of Fe-Mn mineralization? Geol. Soc. Lond., Spec. Publ. 119 (1), 239–251. https://doi.org/10.1144/gsl.sp.1997.119.01.15.

Rey, J., Maestro, A., Somoza, L., Smellie, J.L., 2002. Submarine morphology and seismic stratigraphy of Port Foster. In: López-Martínez, J., Smellie, J.L., Thomson, J.W., Thomson, M.R.A. (Eds.), Geology and Geomorphology of Deception Island. British Antarctic Survey, Cambridge, pp. 40–46 Cambridge, BAS GEOMAP Series, Sheets 6-A and 6-B, 1:25 000.

Riggs, N.R., Duffield, W.A., 2008. Record of complex scoria cone eruptive activity at Red Mountain, Arizona, USA, and implications for monogenetic mafic volcanoes. J. Volcanol. Geotherm. Res. 178 (4), 763–776. https://doi.org/10.1016/j.jvolgeores.2008.09.004.

Roche, O., Druitt, T.H., 2001. Onset of caldera collapse during ignimbrite eruptions. Earth Planet. Sci. Lett. 191 (3–4), 191–202. https://doi.org/10.1016/S0012-821X(01)00428-9.

Roobol, M.J., 1980. A model for the eruptive mechanism of Deception Island from 1820 to 1970. Brit. Antarct. Surv. Bull. 49, 137–156.

Roobol, M.J., 1982. The volcanic hazard at Deception Island, South Shetland Islands. Brit. Antarct. Surv. Bull. 51, 237–245.

Rosado, B., Fernández-Ros, A., Berrocoso, M., Prates, G., Gárate, J., de Gil, A., Geyer, A., 2019. Volcano-tectonic dynamics of Deception Island (Antarctica): 27 years of GPS observations (1991–2018). J. Volcanol. Geotherm. Res. 381, 57–82. https://doi.org/10.1016/j.jvolgeores.2019.05.009.

Ross, P.-S., White, J.D.L., 2012. Quantification of vesicle characteristics in some diatreme-filling deposits, and the explosivity levels of magma–water interactions within diatremes. J. Volcanol. Geotherm. Res. 245–246, 55–67. https://doi.org/10.1016/j.jvolgeores.2012.07.006.

Rull, V., Lara, A., Rubio-Inglés, M.J., Giralt, S., Gonçalves, V., Raposeiro, P., Hernández, A., Sánchez-López, G., Vázquez-Loureiro, D., Bao, R., Masqué, P., Sáez, A., 2017. Vegetation and landscape dynamics under natural and anthropogenic forcing on the Azores Islands: a 700-year pollen record from the São Miguel Island. Quat. Sci. Rev. 159, 155–168. https://doi.org/10.1016/j.quascirev.2017.01.021.

Schaeffer, O.A., Zähringer, J., 1966. Potassium Argon Dating. Springer, Berlin Heidelberg https://doi.org/10.1007/978-3-642-87895-4 246 pp.

Settle, M., 1979. The structure and emplacement of cinder cone fields. Am. J. Sci. 279, 1089–1107. https://doi.org/10.2475/ajs.279.10.1089.

Smellie, J.L., 1988. Recent observations on the volcanic history of Deception Island, South Shetland Islands. Brit. Antarct. Surv. Bull. 81, 83–85.

Smellie, J.L., 2001. Lithostratigraphy and volcanic evolution of Deception Island, South Shetland Islands. Antarct. Sci. 13 (2), 188–209. https://doi.org/10.1017/S0954102001000281.

Smellie, J.L., 2002a. Geology. In: Smellie, J.L., López-Martínez, J., Thomson, J.W., Thomson, M.R.A. (Eds.), Geology and Geomorphology of Deception Island. Cambridge, British Antarctic Survey, Cambridge, pp. 11–30 BAS GEOMAP Series, Sheets 6-A and 6-B, 1:25 000, supplementary text.

Smellie, J.L., 2002b. The 1969 subglacial eruption on Deception Island (Antarctica): events and processes during an eruption beneath a thin glacier and implications for volcanic hazards. In: Smellie, J.L., Chapman, M.G. (Eds.), Volcano-Ice Interactions on Earth and Mars. Geological Society of London, London, pp. 59–79.

Smellie, J.L., 2002c. Volcanic hazard. In: Smellie, J.L., López-Martínez, J., Thomson, J.W., Thomson, M.R.A. (Eds.), Geology and Geomorphology of Deception Island. Cambridge, British Antarctic Survey, Cambridge, pp. 47–53 BAS GEOMAP Series, Sheets 6-A and 6-B, 1:25 000, supplementary text.

Smellie, J.L., 2021. Chapter 3.2a Bransfield Strait and James Ross Island: volcanology. Geological Society, London, Memoirs 55. https://doi.org/10.1144/M55-2018-58 M55-2018–58.

Smellie, J.L., López-Martínez, J., 2002a. Geological and geomorphological evolution: summary. In: Smellie, J.L., López-Martínez, J., Thomson, J.W., Thomson, M.R.A. (Eds.), Geology and Geomorphology of Deception Island. Cambridge, British Antarctic Survey, Cambridge, pp. 54–57 BAS GEOMAP Series, Sheets 6-A and 6-B, 1:25 000, supplementary text.

Smellie, J.L., López-Martínez, J., 2002b. Geological map of Deception Island.Sheet 6A. In: López-Martínez, J., Smellie, J.L., Thomson, J.W., Thomson, M.R.A. (Eds.), Geology and Geomorphology of Deception Island. British Antarctic Survey, Cambridge Cambridge, BAS GEOMAP Series, Sheets 6-A and 6-B, 1:25 000.

Geology and geomorphology of Deception Island. In: Smellie, J.L., López-Martínez, J., Thomson, J.W., Thomson, M.R.A. (Eds.), Geology and Geomorphology of Deception Island. British Antarctic Survey, Cambridge Cambridge: BAS GEOMAP Series, Sheets 6-A and 6-B, 1:25 000, supplementary text. 77 pp.

Solé, J., 2009. Determination of K-Ar ages in milligram samples using an infrared laser for argon extraction. Rapid Commun. Mass Spectrom. 23 (22), 3579–3590. https://doi.org/10.1002/rcm.4280.

Somoza, L., Martínez-Frías, J., Smellie, J.L., Rey, J., Maestro, A., 2004. Evidence for hydrothermal venting and sediment volcanism discharged after recent short-lived volcanic eruptions at Deception Island, Bransfield Strait, Antarctica. Mar. Geol. 203 (1–2), 119–140. https://doi.org/10.1016/S0025-3227(03)00285-8.

Stovall, W.K., Houghton, B.F., Gonnermann, H., Fagents, S.A., Swanson, D.A., 2011. Eruption dynamics of Hawaiian-style fountains: the case study of episode 1 of the Kīlauea Iki 1959 eruption. Bull. Volcanol. 73 (5), 511–529. https://doi.org/10.1007/s00445-010-0426-z.

Stroncik, N.A., Schmincke, H.U., 2002. Palagonite – a review. Int. J. Earth Sci. 91 (4), 680–697. https://doi.org/10.1007/s00531-001-0238-7.

Sumner, J.M., 1998. Formation of clastogenic lava flows during fissure eruption and scoria cone collapse: the 1986 eruption of Izu-Oshima Volcano, eastern Japan. Bull. Volcanol. 60 (3), 195–212. https://doi.org/10.1007/s004450050227.

Torrecillas, C., Berrocoso, M., García-García, A., 2006. The Multidisciplinary Scientific Information Support System (SIMAC) for Deception Island. In: Fütterer, D., Damaske, D., Kleinschmidt, G., Miller, H., Tessensohn, F. (Eds.), Antarctica. Springer, Berlin Heidelberg, pp. 397–402 https://doi.org/10.1007/3-540-32934-x_50.

Torrecillas, C., Berrocoso, M., Felpeto, A., Torrecillas, M.D., Garcia, A., 2013. Reconstructing palaeo-volcanic geometries using a Geodynamic Regression Model (GRM): application to Deception Island volcano (South Shetland Islands, Antarctica). Geomorphology 182, 79–88. https://doi.org/10.1016/j.geomorph.2012.10.032.

Valencio, A., Mendía, E., Vilas, J.F., 1979. Palaeomagnetism and K-Ar age of Mesozoic and Cenozoic igneous rocks from Antarctica. Earth Planet. Sci. Lett. 45, 61–68. https://doi.org/10.1016/0012-821X(79)90107-9.

Valentine, G.A., Krier, D., Perry, F.V., Heiken, G., 2005. Scoria cone construction mechanisms, Lathrop Wells volcano, southern Nevada, USA. Geology 33 (8), 629–632. https://doi.org/10.1130/G21459AR.1.

Vázquez-Loureiro, D., Gonçalves, V., Sáez, A., Hernández, A., Raposeiro, P.M., Giralt, S., Rubio-Inglés, María J., Rull, V., Bao, R., 2019. Diatom-inferred ecological responses of an oceanic lake system to volcanism and anthropogenic perturbations since 1290 CE. Palaeogeogr. Palaeoclimatol. Palaeoecol. 534, 109285. https://doi.org/10.1016/j.palaeo.2019.109285.

Walton, A.W., Schiffman, P., 2003. Alteration of hyaloclastites in the HSDP 2 Phase 1 Drill Core 1. Description and paragenesis. Geochem. Geophys. Geosyst. 4 (5). https://doi.org/10.1029/2002GC000368.

Weiß, B.J., Hübscher, C., Wolf, D., Lüdmann, T., 2015. Submarine explosive volcanism in the southeastern Terceira Rift/São Miguel region (Azores). J. Volcanol. Geotherm. Res. 303, 79–91. https://doi.org/10.1016/j.jvolgeores.2015.07.028.

White, J.D.L., McPhie, J., Soule, S.A., 2015. Submarine lavas and hyaloclastite. The Encyclopedia of Volcanoes. Elsevier, pp. 363–375 https://doi.org/10.1016/b978-0-12-385938-9.00019-5.

Wood, C.A., 1980a. Morphometric analysis of cinder cone degradation. J. Volcanol. Geotherm. Res. 8 (2–4), 137–160. https://doi.org/10.1016/0377-0273(80)90101-8.

Wood, C.A., 1980b. Morphometric evolution of cinder cones. J. Volcanol. Geotherm. Res. 7 (3–4), 387–413. https://doi.org/10.1016/0377-0273(80)90040-2.

Zandomeneghi, D., Barclay, A., Almendros, J., Ibañez Godoy, J.M., Wilcock, W.S.D., Ben-Zvi, T., 2009. Crustal structure of Deception Island volcano from P wave seismic tomography: tectonic and volcanic implications. J. Geophys. Res. 114 (B6), B06310. https://doi.org/10.1029/2008jb006119.

References from the Supporting Information

Chang, L. L. Y., Zussman, J., & Howie, R. A. (1998). *Rock-forming minerals. Vol. 5B, Non-silicates: sulphates, carbonates, phosphates, halides.* (2n Ed.). London: Geological Society of London Pub. House.Deer, W. A., Zussman, J., & Howie, R. A. (2001). *Rock-forming minerals. Vol. 4A, Framework silicate : feldspar* (2nd Ed.). Bath: Geological Society of London Pub. House.Le Bas, M. J., Le Maitre, R. W., Streckeisen, A., Zanettin, B., & Rocks, I. S. on the S. of I. (1986). A Chemical Classification of Volcanic Rocks Based on the Total Alkali-Silica Diagram. *Journal of Petrology*, *27*(3), 745–750. https://doi.org/10.1093/petrology/27.3.745Middlemost, E. A. K. (1989). Iron oxidation ratios, norms and the classification of volcanic rocks. *Chemical Geology*, *77*, 19–26. https://doi.org/10.1016/0009-2541(89)90011-9Morimoto, N. (1988). Nomenclature of Pyroxenes. *Mineralogy and Petrology*, *39*(1), 55–76. https://doi.org/10.1007/BF01226262Hamilton, N. E., & Ferry, M. (2018). ggtern: Ternary Diagrams Using ggplot2. Journal of Statistical Software; Vol 1, Code Snippet 3 (2018). https://doi.org/10.18637/jss.v087.c03Irvine, T. N., & Baragar, W. R. A. (1971). A Guide to the Chemical Classification of the Common Volcanic Rocks. *Canadian Journal of Earth Sciences*, *8*(5), 523–548. https://doi.org/10.1139/e71-055Kusakabe, M., Nagao, K., Ohba, T., Seo, J. H., Park, S.-H., Lee, J. I., & Park, B.-K. (2009). Noble gas and stable isotope geochemistry of thermal fluids from Deception Island, Antarctica. *Antarctic Science*, *21*(3), 255–267. https://doi.org/10.1017/S0954102009001783Geyer, A., Álvarez-Valero, A. M., Gisbert, G., Aulinas, M., Hernández-Barreña, D., Lobo, A., & Marti, J. (2019). Deciphering the evolution of Deception Island's magmatic system. *Scientific Reports*, *9*(1), 373. https://doi.org/10.1038/s41598-018-36188-4R Core Team (2014). R: A language and environment for statistical computing. R Foundation for Statistical Computing, Vienna, Austria. URL http://www.R-project.org/Sun, S. S., & McDonough, W. F. (1989). Chemical and isotopic systematics of oceanic basalts: Implications for mantle composition and processes. *Geological Society Special Publication*, *42*(1), 313–345. https://doi.org/10.1144/GSL.SP.1989.042.01.19Wickham, H. (2009) ggplot2: elegant graphics for data analysis. Springer New York.